NONLINEAR ULTRASONIC GUIDED WAVES FOR QUANTITATIVE LIFE PREDICTION OF STRUCTURES WITH COMPLEX GEOMETRIES

A Thesis
Presented to
The Academic Faculty

by

Thibaut Bernard Autrusson

In Partial Fulfillment
of the Requirements for the Degree
Master of Science in Mechanical Engineering in the
George W. Woodruff School of Mechanical Engineering

Georgia Institute of Technology
December 2009

NONLINEAR ULTRASONIC GUIDED WAVES FOR QUANTITATIVE LIFE PREDICTION OF STRUCTURES WITH COMPLEX GEOMETRIES

Approved by:

Karim G. Sabra
George W. Woodruff School of Mechanical
Engineering
Georgia Institute of Technology

Michael J. Leamy
George W. Woodruff School of Mechanical
Engineering
Georgia Institute of Technology

Laurence J. Jacobs
School of Civil and Environmental
Engineering
Georgia Institute of Technology

Date Approved: October 23, 2009

À mes parents Bruno et Marie-Claude

ACKNOWLEDGEMENTS

First, I would like to thank my advisor Dr. Karim Sabra, whose weekly meetings were an invaluable source of knowledge my for scientific education. He made my stay at the Georgia Institute of Technology very pleasant and stimulating.

My gratefulness goes to my co-thesis advisor Dr. Michael Leamy. Our long discussions allowed me to make strong progress in my research problem, as well as to learn more about computational mechanics. My special thanks to Dr. Jin-Yeon Kim for all his help and support for experiments and data acquisition. Thanks to the committee member Dr. Laurence Jacobs for reviewing this work and giving access to his lab. And thanks to Dr. Jianmin Qu and Dr. Massimo Ruzzene for theoretical and experimental discussions.

At the Ecole Nationale Supérieure de Techniques Avancées (ENSTA ParisTech), I thank Mathieu Le Traon, Director of International Relations, for his help on my application to GeorgiaTech. I also express all my gratitude to the Académie Francaise for awarding me the Jean Walter Zellidja fellowship after my admission at GeorgiaTech.

For the pleasant days we spent together, particularly setting up computers, I would like to thank all my lab mates. Thanks to the administration of George W. Woodruff School of Mechanical Engineering and particularly Dana Foster whose help was essential.

Finally, I would like to thank my family, my twin brother Nicolas, my friends, and Cécile. Their support and encouragements were part of the success of my stay in Atlanta.

TABLE OF CONTENTS

LIST OF TABLES

LIST OF FIGURES

LIST OF SYMBOLS OR ABBREVIATIONS

A, B, C Non-linear Landau and Lifschitz coefficients.

β Normalized non-linear parameter for the P-wave.

c_T Celerity of the shear wave.

curl   Curl.

Δt Time step for two consecutive iterations.

Δx Space resolution along the $x-$axis.

Δy Space resolution along the $y-$axis.

E Young's modulus.

Γ_C Stress boundary.

Γ_D Displacement boundary.

grad   Gradient.

(i, j, k) Subscript localization.

J_{xx} Jacobian matrix of σ_{xx}.

λ Lamé coefficient.

Λ_1 Linear elastic tensor.

Λ_2 Non-linear elastic tensor.

l, m, n Non-linear coefficients.

L_x Dimension along the $x-$axis.

L_y Dimension along the $y-$axis.

μ Lamé coefficient.

∇ Nabla operator.

$\nabla^2(\cdot)$ Laplacian.

N_x Length of the grid along the $x-$axis.

N_y Length of the grid along the $y-$axis.

$\partial\Omega$ Boundary of the volume Ω.

PDE	Partial differential equation.
ψ	Displacement vector potential.
ρ	Mass density.
$\rho_0 W$	strain energy.
SE	Squared error.
σ	Stress.
$\tilde{f}$	Numerical solution.
u	Displacement.
Υ	Excitation function.
ε	Strain.
φ	Displacement potential.
$_{,x}$	Derivation with respect to the x direction.

SUMMARY

This research investigates the possibilities of simulating the wave propagation in a solid complex medium. Non-linear behavior of the material is studied through a model that considers the classical Hooke's law with quadratic terms. In addition to the Lamé coefficients the Landau and Lifschitz coefficients are introduced to characterized the non-linearities. As well as theory a short experiment is presented to highlight the signal processing for such as material model.

In the next chapter, Cellular Automata (CA) is introduced as a new simulation method, in order to develop new analysis on non-linearities. Starting from an existing linear code, this one is progressively modified to take into account a different Hooke's law. Theoretical results and numerical results are presented in order to make robust code. Thus, stability of the linear code is proved using von Neumann analysis.

The propagation of the P-wave is investigated in detail. This work provides verification for the accuracy by comparison of a closed form solution and the corresponding computational solution. Also rules are established in order to get good parameters for the size of the grid and the time step. Then these methods are applied for the non-linear code, and provide accuracy as well.

Finally the capabilities of the Cellular Automata code are underlined for simulating Lamb waves in a linear material. Because these waves are essential in structural health monitoring (SHM) with complex geometries, simulation and quantification of the reflection of the $A1$ mode are provided.

CHAPTER I

INTRODUCTION

Ultrasonic measurement techniques have recently been shown to detect fatigue in metallic structure. Classic non-destructive evaluation (NDE) uses linear measurement. Indeed it is possible to detect a macroscopic crack in a material with techniques such as beamforming with an array of piezoelectric sensors that analyze the scattered wavefield emanating from the crack [1]. However these techniques are not appropriate for measuring microcracks because their influence is too small on the linear wave. But accumulation of these nascent cracks leads to non-linear behavior of the material which distorts propagating waves by adding a higher harmonic component in the spectrum [4, 10]. Thus the non-linear ultrasonic wave component could allow to quantify the crack density and then early stages of fatigue, because increase of material non-linearity have been related to increase in fatigue damage [10]. This model can be also applied on damaged zones exhibiting plasticity.

Moreover the geometry is an important factor to take into account. The material have finite length which implies the existence of reflections from the edges. Also theoretical and technical results on the ideal plate geometry [1] cannot be applied to other types of forms. It emphasizes the need for numerical simulations in order to predict such a non-linear behavior in complicated geometry.

The theory of non-linear elasticity is reviewed in the second chapter. Non-linearities can be included in the stress-strain relationship through the standard Landau and Lifschitz coefficients [11], equivalent to the Lamé coefficients. This formulation provides an extension of the Hooke's law with quadratic terms. The third chapter is dedicated to the Cellular Automata (CA) numerical code that was developed for solving

non-linear elastic wave propagation in 2D dimension. CA is a novel approach for computational mechanics especially suited for elastic wave propagation in complex domain [3]. The CA formulation has the advantage of being directly based on the physics of the model and the constitutive relationships for the material. Hence the CA formulation differs from other numerical methods, such as, finite differences or finite elements are based instead on discretizing the continuous wave equation on a grid to solve it numerically. Starting from an existing CA code on linear mechanics [3], theoretical work is presented. Stability considerations are explored in details in order to underline the robustness of the CA formulation. A method is proposed for verifying the linear code accuracy, by introducing computational error. This first use of the CA code is also the occasion to establish rules for the computational parameters such as the size of the cells and the time step. As well as the field equations, the boundary conditions were reviewed to take into account a non-linear material, propositions were develop to ensure the uniqueness of the computational solution.

After implementing the non-linear behavior in the CA code, verifications are necessary to validate the new code on simple geometry. The numerical predictions were subsequently compared to first order theoretical predictions for a propagating one-dimensional P-wave [16]. Guided waves such as Rayleigh or Lamb waves, travel on long distance providing a tool for large area inspection. The Rayleigh wave propagates along a free surface and thus may investigate the edges of a given material. The Lamb waves consists in a mode that propagates in a plate structure for instance. Different options are presented for the external forcing that will generate such a wave in a thin structure. Also this will be the occasion to test the code again. Particularly, the dispersion curves of the Lamb are derived from CA simulation and signal processing. The reflections of the $A1$ mode on a free edge are presented as well. A quantification of the amplitude was compared for the incident and reflected wave at different frequencies. This computation can be reproduced on real experiments and

emphasize the direct correlation of simulation and practical aspect. The sixth chapter concludes the work done in this thesis and provides perspectives for future work. As an appendix, a computer program is briefly presented in order to underscore the necessity of processing efficiently raw data from CA computation.

CHAPTER II

NON-LINEAR ELASTICITY

This chapter outlines the theory of material elasticity for isotropic and homogeneous material. From this theory, linear elasticity may be derived and a more general approach leads to non-linear elasticity. At this point, the Landau and Lifschitz coefficients are introduced as an extension of the Lamé coefficients for non-linear formulation. The whole computation of the stress tensor is provided for the two-dimensional case, and an extension to linearization is presented as well. In order to emphasize the possibilities of such a material model an experiment is presented as a way to measure material non-linearities. Theoretical results are presented along this chapter as a basis for next chapters.

2.1 Non-linear Hooke's law

Based on a parallel between linear and non-linear equations, the non-linear Hooke's law is progressively introduced. Discussion includes strain energy because it gives an easy way to understand non-linear coefficients.

2.1.1 The strain energy

We begin with the canonical beam as an illustrative example. On the right side a constraint σ is applied while it is clamped on the left side, as depicted on figure 1. The behavior of a given material is describe by a constitutive relationship. In this case the 1D Hooke's law is the suitable description,

$$\sigma = E\varepsilon, \tag{1}$$

where ε is the strain and E the Young's modulus.
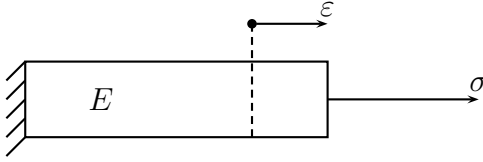
Figure 1: A beam clamped on the left side and pulled by a constraint σ on the right side. It strain follows to the one dimensional Hooke's law (Eq. 1), with a Young's modulus equals to E.
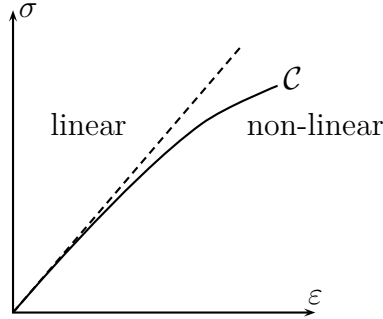
Figure 2: Stress-Strain curve $\mathcal{C}$ for a given material.

For non-linear elasticity it is necessary to consider a more general constitutive equation instead of Eq. 1. In doing so, it must take into account a quadratic term in ε^2. A natural generalization would be higher order polynomial, as exhibited by,

$$\sigma = E\varepsilon + \frac{1}{2}E'\varepsilon^2, \tag{2}$$

where E is known as the Young modulus and E' is the curvature of the function $\sigma : \varepsilon \rightarrow \sigma(\varepsilon)$. The graph of this function is the stress-strain curve on figure 2. Due to $\varepsilon \ll 1$ the quadratic term is very small compared to linear term and Taylor expansion will be limited to the second order. Then the higher order terms will not be considered. Moreover the material will always be considered to be elastic. Thus after a stress occurred on the structure, it will return to its original shape. Mathematically $(\sigma, \varepsilon) \in \mathcal{C}$, which means the material always follows the stress-strain curve $\mathcal{C}$, which is not connected.

To obtain the non-linear elasticity law in terms of tensors, it is necessary to modify

Eq. 2. The stress tensor $\underline{\underline{\sigma}}$ has, then, the following expression,

$$\underline{\underline{\sigma}} = \underline{\underline{\underline{\underline{\Lambda_1}}}} : \underline{\underline{\varepsilon}} + \frac{1}{2} \, \underline{\underline{\varepsilon}} \cdot \underline{\underline{\underline{\underline{\Lambda_2}}}} \cdot \underline{\underline{\varepsilon}}, \tag{3}$$

where "$\cdot$" (resp. "$:$") stands for the simple (resp. double) contracted product of two tensors. The linear elastic tensor Λ_1 is already known. It contains either the Lamé coefficients or the Poisson's ratio and Young's modulus. The non-linear elastic tensor Λ_2 contains also some constants. Energy considerations will help to find these constants.

The compatibility equation makes the link between the displacement and the strain. This relation is linear,

$$\underline{\underline{\varepsilon}} = \frac{1}{2} \left(\underline{\underline{\nabla}} \, \underline{u} + \underline{\underline{\nabla}}^{\mathrm{T}} \underline{u} \right), \tag{4}$$

In the expression 4, the non-linear geometric terms are neglected because the displacement u are considered to be small. Indeed vibrations in solid always implies small displacements. However in non-linear acoustics, the assumption may not be valid anymore because displacement can be larger.

The tensor $\underline{\underline{\underline{\underline{\Lambda_2}}}}$ comes from the expression of the strain energy $\rho_0 W$. Indeed $\underline{\underline{\sigma}}$ is defined as the derivative [13] of this energy with respect to $\underline{\underline{\varepsilon}}$,

$$\underline{\underline{\sigma}} = \rho_0 \frac{dW}{d\underline{\underline{\varepsilon}}} \tag{5}$$

$$\text{or,} \qquad \sigma_{ij} = \rho_0 \frac{dW}{d\varepsilon_{ij}}. \tag{6}$$

The expression of the strain energy $\rho_0 W$ is assumed to come from Taylor expansion,

$$\rho_0 W = \frac{1}{2!} D_{ijkl} \varepsilon_{ij} \varepsilon_{kl} + \frac{1}{3!} D_{ijklmn} \varepsilon_{ij} \varepsilon_{kl} \varepsilon_{mn} + \cdots . \tag{7}$$

Non-linear elasticity extends the expression of the strain energy through the third order terms. The Eq. 7 is very general but it does not take into account the proprieties of the material, typically isotropy or homogeneity. If it satisfies both assumptions,

an easy way to find how many constants are necessary to describe the tensor $\underline{\underline{\Lambda_2}}$, is to use another expression for W, with its invariants. Because the material has the same physical proprieties at every point in every directions, it should depend only on its invariants, I_1, I_2 and I_3. Thus polynomial expression in Eq. 7 becomes,

$$\rho_0 W = \sum_{ijk} c_{ijk}(I_1 - 1)^i (I_2 - 1)^j (I_3 - 1)^k, \tag{8}$$

where,

$$I_1 = \text{tr } \underline{\underline{\varepsilon}}, \tag{9}$$

$$I_2 = \frac{1}{2}\left((\text{tr } \underline{\underline{\varepsilon}})^2 - \text{tr } \underline{\underline{\varepsilon}}^2\right), \tag{10}$$

$$I_3 = \det \underline{\underline{\varepsilon}}. \tag{11}$$

The I_i are homogeneous polynomials of degree i in ε_{ij}. For instance the term I_2 has degree 2 because it is made of a sum of $\varepsilon_{ij}\varepsilon_{kl}$. A closer look at Eq. 8 shows that only three terms have degree 3. They are obtained for $(i, j, k) = (3, 0, 0)$ or $(0, 0, 1)$ or $(1, 2, 0)$. Therefore $\underline{\underline{\Lambda_2}}$ contains three independent constants. These coefficients are the standard A, B, C or l, m, n, according to Landau and Lifschitz in [11].

A possible expression for W (see also [6]), only using the trace of the tensor, is

$$\rho_0 W(\underline{\underline{\varepsilon}}) = \frac{\lambda}{2}(\text{tr}\underline{\underline{\varepsilon}})^2 + \mu \text{ tr}\underline{\underline{\varepsilon}}^2 + \frac{C}{3}(\text{tr}\underline{\underline{\varepsilon}})^3 + B(\text{tr}\underline{\underline{\varepsilon}})\text{tr}\underline{\underline{\varepsilon}}^2 + \frac{A}{3}\text{tr}\underline{\underline{\varepsilon}}^3, \tag{12}$$

where $\underline{\underline{\varepsilon}}^2 = \underline{\underline{\varepsilon}}\,\underline{\underline{\varepsilon}}$, is the matrix product. There exists another expression for the strain energy, given in [14] by McCall. This time the expression contains the three constant (l, m, n),

$$\rho_0 W(\underline{\underline{\varepsilon}}) = \frac{\lambda + 2\mu}{2}I_1^2 - 2\mu I_2 + \frac{l + 2m}{3}I_1^3 - 2mI_1 I_2 + nI_3. \tag{13}$$

2.1.2 Relationship between non-linear coefficients

The previous has underlined several equivalent expressions for the strain energy. Each of these expressions uses a different set coefficients (l, m, n) or (A, B, C) or D_{ijklmn}.

Because the reader may find these coefficients in the literature, the link between the coefficients is stated here. This paragraph relies on the work of Norris [9], in which he defines the D_{ijklmn} from Eq. 7, as

$$D_{ijklmn} = 2C\delta_{ij}\delta_{kl}\delta_{mn} + 2B(\delta_{ij}I_{klmn} + \delta_{kl}I_{mnij} + \delta_{mn}I_{ijkl})$$
$$+A/2(\delta_{ik}I_{jlmn} + \delta_{il}I_{jkmn} + \delta_{jk}I_{ilmn} + \delta_{jl}I_{ikmn}),$$

where $I_{ijkl} = (\delta_{ik}\delta_{jl} + \delta_{il}\delta_{jk})/2$.

Secondly, one may write the expression $\det \underline{\underline{\varepsilon}}$ in terms of $\mathrm{tr}\underline{\underline{\varepsilon}}$, $\mathrm{tr}\underline{\underline{\varepsilon}}^2$ and $\mathrm{tr}\underline{\underline{\varepsilon}}^3$.

$$\mathrm{tr}\ \underline{\underline{\varepsilon}} = I_1 \tag{14}$$

$$\mathrm{tr}\ \underline{\underline{\varepsilon}}^2 = I_1^2 - 2I_2 \tag{15}$$

$$\mathrm{tr}\ \underline{\underline{\varepsilon}}^3 = I_1^3 - 3(I_1 I_2 - I_3) \tag{16}$$

After plugging back these equations in Eq. 12, it comes,

$$A = n \tag{17}$$

$$B = -m - \frac{1}{2}n \tag{18}$$

$$C = 3l + \frac{3}{2}m + \frac{1}{2}n. \tag{19}$$

Henceforth the coefficients (A, B, C) are chosen arbitrarily.

2.2   The 2D case

2.2.1   The non-linear stress tensor

From 3D theory the expression of Hooke's law is derived in two dimensions. The stress tensor is computed from Eq. 6. The component on the third dimension, i.e. $z-$axis, is not explored. Therefore the only interesting stress components are $(\sigma_{xx}, \sigma_{yy}, \sigma_{xy})$. Because W is the sum of linear terms and non-linear terms it is also possible to separate $\underline{\underline{\sigma}}$ into two different terms.

$$\underline{\underline{\sigma}} = \underline{\underline{\sigma}}^{\text{linear}} + \underline{\underline{\sigma}}^{\text{non-linear}}. \tag{20}$$

The first term is

$$
\begin{pmatrix} \sigma_{xx} \\ \sigma_{yy} \\ \sigma_{xy} \end{pmatrix}^{\text{linear}} = \begin{pmatrix} \lambda + 2\mu & \lambda & 0 \\ \lambda & \lambda + 2\mu & 0 \\ 0 & 0 & 2\mu \end{pmatrix} \begin{pmatrix} \varepsilon_{xx} \\ \varepsilon_{yy} \\ \varepsilon_{xy} \end{pmatrix},
\tag{21}
$$

while the second term is,

$$
\sigma_{xx}^{\text{non-linear}} = \varepsilon_{xx}^2 (A + 3B + C) + (B + C)\varepsilon_{yy}^2 + \varepsilon_{xy}^2 (A + 2B) + \varepsilon_{xx}\varepsilon_{yy}(2C + 2B) \tag{22a}
$$

$$
\sigma_{yy}^{\text{non-linear}} = \varepsilon_{xx}^2 (B + C) + \varepsilon_{yy}^2 (A + 3B + C) + \varepsilon_{xy}^2 (A + 2B) + \varepsilon_{xx}\varepsilon_{yy}(2C + 2B) \tag{22b}
$$

$$
\sigma_{xy}^{\text{non-linear}} = \varepsilon_{xx}\varepsilon_{xy}(2B + A) + \varepsilon_{yy}\varepsilon_{xy}(2B + A). \tag{22c}
$$

2.2.2 Linearized equations

Because the non-linear equations are not easy to manipulate, an alternative approach is provided. If one desires to work in a region close to the point $(\bar{\varepsilon}, \sigma(\bar{\varepsilon}))$ he may not require the full extent of the non-linear law. To obtain a linear law, one way to approximate $\sigma(\varepsilon)$ by its tangent $\tilde{\sigma}(\varepsilon)$ at point $(\bar{\varepsilon}, \sigma(\bar{\varepsilon}))$. The tangent of the expression 2 is given below,

$$
\tilde{\sigma}(\varepsilon) = \underbrace{(E + E'\varepsilon)}_{\mathrm{d}\sigma/\mathrm{d}\varepsilon} \underbrace{(\varepsilon - \bar{\varepsilon})}_{\Delta\varepsilon} + \underbrace{\left(E\bar{\varepsilon} + \frac{1}{2}E'\bar{\varepsilon}^2 \right)}_{\sigma(\bar{\varepsilon})}.
\tag{23}
$$

Note that $\tilde{\sigma}(\cdot)$ could also be written as a function of $\Delta\varepsilon$ instead of ε. The approximation described above is represented on the figure 3. In addition this figure represents a validity domain $\mathcal{D}$. This point will not be discussed but it is obvious that if one wants to use a valid approach he must give a validity domain with his approximation. After studying the 1D case, the linearized the 2D case is explained. In theory and with the same notations as on the figure 3,

$$
\tilde{\sigma}(\Delta\varepsilon) = \frac{\partial\sigma}{\partial\varepsilon}(\bar{\varepsilon}) \cdot \Delta\varepsilon + \sigma(\bar{\varepsilon}).
\tag{24}
$$

With two dimensions the derivative is replaced by the Jacobian matrix. For σ_{xx} the Jacobian is $J_{xx} \in \mathcal{M}_{13}(\mathbb{R})$, because σ_{xx} is a function of three variables $(\varepsilon_{xx}, \varepsilon_{yy}, \varepsilon_{xy})$.

9
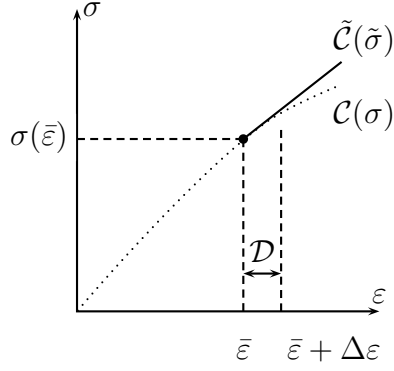
Figure 3: Stress-Strain approximation $\tilde{\mathcal{C}}$ of $\mathcal{C}$, and $\mathcal{D}$ validity domain

The approximated linear solution is then,

$$\tilde{\sigma}_{xx}(\Delta\varepsilon_{xx}, \Delta\varepsilon_{xx}, \Delta\varepsilon_{xx}) = J_{xx}(\bar{\varepsilon}_{xx}, \bar{\varepsilon}_{yy}, \bar{\varepsilon}_{xy}) \begin{pmatrix} \Delta\varepsilon_{xx} \\ \Delta\varepsilon_{yy} \\ \Delta\varepsilon_{xy} \end{pmatrix} + \sigma_{xx}(\bar{\varepsilon}_{xx}, \bar{\varepsilon}_{yy}, \bar{\varepsilon}_{xy}), \qquad (25)$$

and,

$$J_{xx}(\bar{\varepsilon}_{xx}, \bar{\varepsilon}_{yy}, \bar{\varepsilon}_{xy}) = \left(\frac{\partial\sigma_{xx}}{\partial\varepsilon_{xx}}, \frac{\partial\sigma_{xx}}{\partial\varepsilon_{yy}}, \frac{\partial\sigma_{xx}}{\partial\varepsilon_{xy}} \right) (\bar{\varepsilon}_{xx}, \bar{\varepsilon}_{yy}, \bar{\varepsilon}_{xy}) \qquad (26)$$

Explicit computation of J_{xx} is

$$J_{xx}^{\mathrm{T}} = \begin{pmatrix} \lambda + 2\mu + 2\bar{\varepsilon}_{xx}(A + 3B + C) + \bar{\varepsilon}_{yy}(2B + 2C) \\ \lambda + 2\bar{\varepsilon}_{yy}(B + C) + 2\bar{\varepsilon}_{xx}(B + C) \\ 2\bar{\varepsilon}_{xy}(A + 2B), \end{pmatrix} \qquad (27)$$

hence,

$$\tilde{\sigma}_{xx}(\Delta\underline{\varepsilon}) = \begin{pmatrix} \lambda + 2\mu + 2\bar{\varepsilon}_{xx}(A + 3B + C) + \bar{\varepsilon}_{yy}(2B + 2C) \\ \lambda + 2\bar{\varepsilon}_{yy}(B + C) + 2\bar{\varepsilon}_{xx}(B + C) \\ 2\bar{\varepsilon}_{xy}(A + 2B) \end{pmatrix}^{\mathrm{T}} \begin{pmatrix} \Delta\varepsilon_{xx} \\ \Delta\varepsilon_{yy} \\ \Delta\varepsilon_{xy} \end{pmatrix} + \sigma_{xx}(\bar{\underline{\varepsilon}}),$$

$$(28)$$

where $\sigma_{xx}(\bar{\underline{\varepsilon}})$ is given by Eq. 20. In the same way it is possible to compute the terms

$\tilde{\sigma}_{yy}$ and $\tilde{\sigma}_{xy}$,

$$\tilde{\sigma}_{yy}(\Delta\underline{\underline{\varepsilon}}) = \begin{pmatrix} \lambda + 2\bar{\varepsilon}_{xx}(B+C) + 2\bar{\varepsilon}_{yy}(B+C) \\ \lambda + 2\mu + 2\bar{\varepsilon}_{xx}(A+3B+C) + \bar{\varepsilon}_{yy}(2B+2C) \\ 2\bar{\varepsilon}_{xy}(A+2B) \end{pmatrix}^{\mathrm{T}} \begin{pmatrix} \Delta\varepsilon_{xx} \\ \Delta\varepsilon_{yy} \\ \Delta\varepsilon_{xy} \end{pmatrix} + \sigma_{yy}(\bar{\bar{\varepsilon}}),$$

(29)

and,

$$\tilde{\sigma}_{xy}(\Delta\underline{\underline{\varepsilon}}) = \begin{pmatrix} \bar{\varepsilon}_{xy}(A+2B) \\ \bar{\varepsilon}_{xy}(A+2B) \\ 2\mu + (\bar{\varepsilon}_{xx} + \bar{\varepsilon}_{yy})(A+2B) \end{pmatrix}^{\mathrm{T}} \begin{pmatrix} \Delta\varepsilon_{xx} \\ \Delta\varepsilon_{yy} \\ \Delta\varepsilon_{xy} \end{pmatrix} + \sigma_{xy}(\bar{\bar{\varepsilon}}).$$

(30)

This completes the theory of non-linear elasticity in two dimensions.

2.3   Non-linearities visible under simple experiment

This section outlines experiments which demonstrate the existence of non-linearities and one way to measure those. The experimental set-up is presented as well as signal processing and results. The sample used is made of aluminum broken under traction cycles. Under these conditions the fatigue is assumed to be important as well as the non-linearities in the material.

2.3.1   Observation

As previously mentioned, the affect of non-linearities is weak relative to the linear behavior. Thus an experiment must involve a physical phenomenon with a suitably small characteristic length. Therefore wave propagation is preferred, because the wave length is much smaller than any other length here.

2.3.1.1   Experimental set-up

The experiment is performed as described on the Fig. 4. The plastic and damaged zone is assumed to give a non-linear behavior.
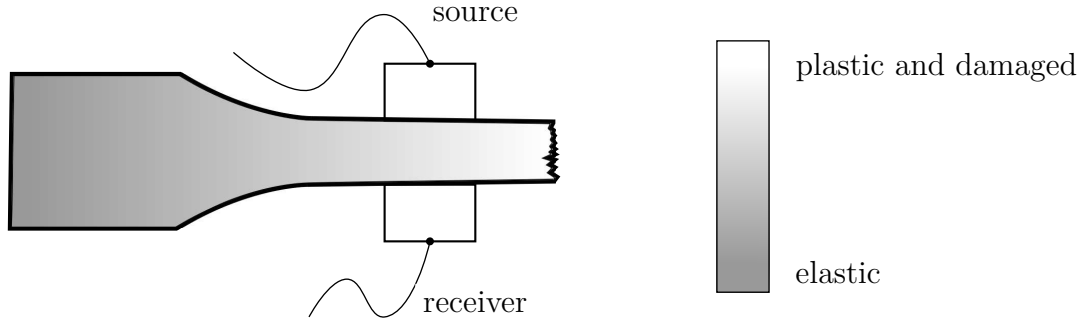
Figure 4: Experimental set-up on a fractured material sample for detection of non-linearities. The source is a piezo-electric oscillating at the frequency 5 MHz. Qualitative assessment of damage along the sample is also indicated.

This experiment largely follows the procedure of article [10]. A transducer vibrating at 5 MHz is placed on the top, and a receiver is located on the opposite side. The two electronic devices are held firmly with a clamp. To help the transmission of energy, the surface between sensors and the material has been lubricated with oil. The signal comes from a wave form generator, then goes through an amplifier and eventually to the piezo-electric sensor. This signal is monitored with an oscilloscope. The source consists in a sinusoid of 9 cycles, allowing to separate first arrival and echoes at the receiver.

2.3.1.2 Digital signal processing

The signal from the receiver is sampled by an oscilloscope and digitally saved. The sample frequency is high enough (100 MHz), to catch non-linear phenomenon. Indeed the non-linear signal has the frequency 10MHz. The Nyquist's sampling theorem implies to sample at least 20MHz but 100MHz allows a good time resolution. In order to underlines characteristics of the recorded signal, noted $s(t)$, it is submitted to different linear transformations.

1. A frame is selected with a Hanning (Hann.) window $Y(t)$. For instance the first

arrival can be isolated from echoes.

$$s(t) \xrightarrow{\text{Hann.}} Y(t)s(t)$$

2. Because interesting frequencies are 5MHz and 10Mhz, a Butterworth filter (Butte.) $h(t)$ is applied to select the band pass between 2Mhz and 13Mhz. The rest of the signal is noise due to electronics or third order non-linearities if they exist.

$$Y(t)s(t) \xrightarrow{\text{Butte.}} h(t) * Y(t)s(t)$$

3. The Discrete Fourier transform ($\mathcal{F}$) is computed with the FFT. This is method allows to separate different frequencies components ,the linear response at 5 MHz and the non-linear response at 10 MHz.

$$h(t) * Y(t)s(t) \xrightarrow{\mathcal{F}} \widehat{h}(f) \times \widehat{Y \cdot s}(f)$$

2.3.1.3   Results and heuristic

The result obtained after all that procedure is the spectrum depicted on Fig. 5. As expected a peak at 5 MHz corresponds to the main external forcing by the piezo-electric, and a second small peak at 10 MHz. This peak is characteristic of a non-linear behavior. This experiment reveals that it is possible to observed non-linearity in a broken and plastic material. The weakness of non-linearities has also been observed.

A heuristic is given below as a short explanation of the experimental result. The signal received u_{received} is assumed to be quadratic function of the source signal, $u_{\text{source}} = u_0 \cos(\omega t)$,

$$u_{\text{received}} = \zeta u_{\text{source}} + \eta \left(u_{\text{source}}\right)^2. \tag{31}$$

After expanding the expression 31, it comes

$$u_{\text{received}} = \underbrace{\frac{\eta}{2}}_{\text{filtered}} + \zeta u_0 \cos(\omega t) + \frac{\eta}{2} u_0 \cos(2\omega t). \tag{32}$$

13
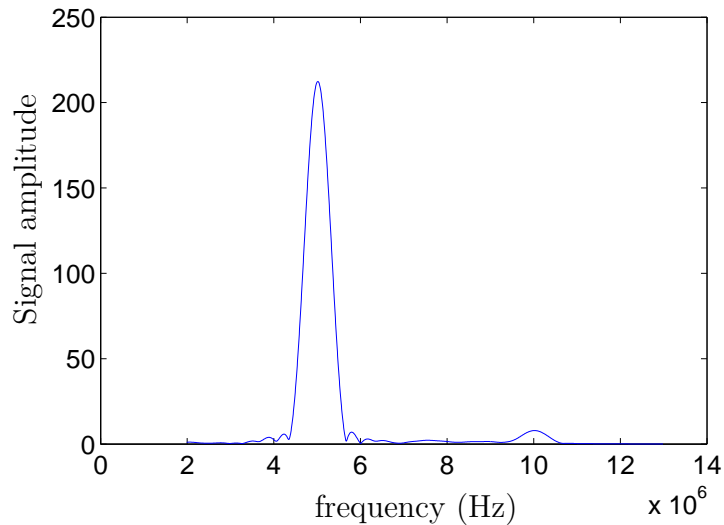
Figure 5: Spectrum of the signal after signal processing and propagation through a non-linear material. The biggest peak corresponds to the external forcing of the piezo-electric. Secondary peak emphasizes non-linearity.

This heuristic shows that the non-linear effect produced a second harmonic at twice the original frequency. Note, Fig. 5 does not shows any terms at zero frequency because of the bandpass filter used in signal processing. This experiment gives an introduction to possible techniques in order to monitor non-linearities. In [10] authors emphasize the link between fatigue and non-linearity. Hence non-linearity and wave propagation may offer perspectives for SHM.

2.3.2 Solution for the non-linear 2D problem

In this paragraph the case of a semi-infinite medium, submitted to an external forcing on its upper boundary, is explored. The previous heuristic is fully explained, here, in mathematical terms, with a closed form solution.

Due to symmetry, the variable x does not appear in the expressions below. This gives a nice perspective to study the analytical problem. By this assumption the displacement in the material is along the $y-$axis, making the displacement $\vec{u}(x, y, t) = u(y, t)\vec{y}$. In other words the elastic wave travels in the material as a longitudinal P-wave. Indeed the displacement is colinear to the wave vector. A consequence

14
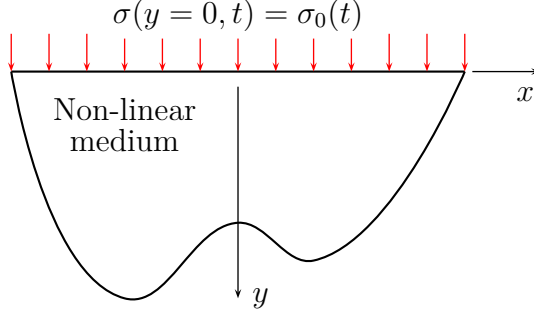
Figure 6: Semi infinite non-linear medium

of that displacement is $\varepsilon_{xx} = \varepsilon_{xy} = 0$. The wave equation is derived from the three fundamental equations. First, using the non-linear Hooke's law of the previous chapter we can write the stress as,

$$\sigma_{xx} = \lambda\varepsilon_{yy} + (B+C)\varepsilon_{yy}^2 \tag{33}$$

$$\sigma_{yy} = (\lambda + 2\mu)\varepsilon_{yy} + (A + 3B + C)\varepsilon_{yy}^2 \tag{34}$$

$$\sigma_{xy} = 0 \tag{35}$$

where the strain ε_{yy} is

$$\varepsilon_{yy} = \frac{\partial u}{\partial y}. \tag{36}$$

Third, the second Newton's law applied on a particle of density ρ, without external forces is

$$\mathrm{div}\sigma = \rho\frac{\partial^2 u}{\partial t^2}. \tag{37}$$

After combining the different equations in order to obtain a unique equation on the displacement, the non-linear wave equation (the other equation gives a triviality) gives,

$$\rho\frac{\partial^2 u}{\partial t^2} = (\lambda + 2\mu)\frac{\partial^2 u}{\partial y^2} + 2(A + 3B + C)\frac{\partial^2 u}{\partial y^2}\frac{\partial u}{\partial y}. \tag{38}$$

In the previous Eq. 38, if $A = B = C = 0$ the linear equation is rendered. Thus it is convenient to continue using the celerity of the P-wave, $c_P^2 = (\lambda + 2\mu)/\rho$. Another interesting quantity is the ratio β, of non-linear material coefficient to linear coefficient.

The equation above becomes

$$\frac{\partial^2 u}{\partial^2} = c_P^2 \frac{\partial^2 u}{\partial y^2} + c_P^2 \underbrace{\frac{2(A+3B+C)}{\lambda+2\mu}}_{\beta} \frac{\partial^2 u}{\partial y^2}\frac{\partial u}{\partial y}. \tag{39}$$

A new assumption is required here to find a solution. The displacement is the sum of two functions. One represents the linear term and the second one the non linear term,

$$u(y,t) = u_1(y,t) + u_2(y,t). \tag{40}$$

The amplitude follows $\sup|u_2| \ll \sup|u_1|$, conforming to the perturbation method. This assumption as been verified on the previous experiment. Indeed Fig. 5 depicts the non-linear term is approximatively 1% of the linear solution. Then u_1 is considered to have order 0 while u_2 has order 1. The problem has now two unknown functions yet to be determined. Thus in order to form a system of two equations expression 40 is plugged back in the Eq. 39. From this equation the separation of orders 0 and 1 yields two equations. Terms of higher orders 2, 3, ... are neglected.

This gives two equations,

$$\frac{\partial^2 u_1}{\partial t^2} = c_P^2 \frac{\partial^2 u_1}{\partial y^2}, \tag{41}$$

$$\frac{\partial^2 u_2}{\partial t^2} = c_P^2 \frac{\partial^2 u_2}{\partial y^2} + c_P^2 \beta \frac{\partial^2 u_1}{\partial y^2}\frac{\partial u_1}{\partial y}. \tag{42}$$

For a wave with a cosine shape, it is

$$u_1(y,t) = Q\cos(ky - \omega t) \tag{43}$$

$$\frac{\partial^2 u_2}{\partial t^2} - c_P^2 \frac{\partial^2 u_2}{\partial y^2} = \frac{1}{2} c_P^2 \beta Q^2 k^3 \sin(2ky - 2\omega t). \tag{44}$$

One may easily verify that the solution for the displacement is

$$u_2(y,t) = -y\frac{1}{8}\beta k^2 Q^2 \left(1 - \cos(2ky - 2\omega t)\right) + f(y,t), \tag{45}$$

and,

$$u(y,t) = Q\cos(ky - \omega t) - y\frac{1}{8}\beta k^2 Q^2 \left(1 - \cos(2ky - 2\omega t)\right) + f(y,t). \tag{46}$$

16

f is an unknown function determined by the boundary conditions at $y = 0$. Thus for an excitation, at the boundary $y = 0$, written as $\sigma_0(t) = -P\sin(\omega t)$, the general solution is

$$u(y,t) = \frac{P}{k(\lambda + 2\mu)}\left(1 - \cos(\omega t - ky)\right) - \frac{\beta P^2}{16k(\lambda + 2\mu)^2}\sin(2\omega t - 2ky)$$
$$+ \frac{\beta c_P P^2}{4(\lambda + 2\mu)^2}(t - y/c_P) + \frac{\beta P^2}{8(\lambda + 2\mu)^2}y\cos(2\omega t - 2ky). \qquad (47)$$

The link with the amplitude Q is $Q = -P/k(\lambda + 2\mu)$. The solution [5] given above without further mathematical derivation. The first term corresponds to u_1 and the other terms correspond to u_2. A growing linear term is contained in u_2 and suggests infinite energy. However this solution is based on the fundamental assumption $\sup|u_2| \ll \sup|u_1|$. As such, when the growing term is too big the model is not valid anymore. A criterion for the Eq. 47 to be valid is then written below. Three terms have order 0 and one term has order 1. Then each of the three 0 order term must be compared to the only term in order 1.

This first criterion is,
$$\frac{\beta P}{16(\lambda + 2\mu)} \ll 1.$$

The last equation is usually verified because the Lamé coefficients are always much larger than the applied load. The second and third criterion are the same,
$$\frac{\beta P^2}{8(\lambda + 2\mu)^2}y \ll \frac{P}{k(\lambda + 2\mu)}$$
$$y \ll \frac{4}{\beta k}\frac{\lambda + 2\mu}{P}.$$

Thus the previous criteria are reformulated in proposition 2.3.1 as only one criterion.

Proposition 2.3.1. *Eq. 47 is a valid solution for the P-wave in a non-linear material if*

$$|y| < L^* \qquad (48)$$

is satisfied, with

$$L^* = \frac{4}{10\beta k}\frac{\lambda + 2\mu}{P}$$

17

It is necessary to evaluate roughly this length L^* for further experiments. The parameters are $\beta \approx 1$, for aluminum $\lambda + 2\mu \approx 10^{11}$ Pa, for experiment at 5 MHz $k \approx 10^3$ m^{-1} and if $P = 10^6$ Pa then $L^* = 1$ m. The physical experiment satisfies this criteria because the spectrum shows that the non-linear component is much smaller than the linear one as depicted on Fig. 5. Also, the distance traveled by the wave is small even after several reflections.

2.3.3 Conclusion

This chapter shows that damaged material provides non-linearities on waves traveling inside itself. As demonstrated, the non-linearities are growing proportional to the thickness of the material. Observation of such a wave can be done with Fourier transform to separate the fundamental and harmonic frequencies.

CHAPTER III

CELLULAR AUTOMATA METHOD FOR SIMULATION OF WAVE PROPAGATION

3.1 *Introduction*

The Cellular Automata (CA) method considers a material domain divided into finite state variables called cells and the state of each cell is updated according to local rules at every discrete time step. More precisely the state for each cell (i.e. displacement, velocity, stress on its boundary) is governed by local equilibrium with adjacent cells, see Fig. 7. From this local approach emerges a global behavior. In [12] Leamy shows the correspondence between continuous model and CA formulation. This posteriori correspondence allows to compute the solution of the wave equations in arbitrary geometry for material having complex constitutive relationships and rheological laws.

3.1.1 Algorithm

The starting point of the CA code is the system of three equations necessary to form the wave equations, Newton's second law, Hooke's law and compatibility equation. In the continuous domain a particle of dimensions $dx \times dy$ is considered. dx is a differential and thus has no extent. The main idea of CA is to replace that differential dx by some length Δx, and develop discrete equations. These will rule the interactions of one cell and its neighbors.

On the contrary, finite difference scheme consists in descretizing the wave equations i.e. the partial differential equations (PDE) on a squared grid. From that point of view the cellular automata is a generalization of the finite difference method, because it works directly on constitutive equations. The cells may have different shapes
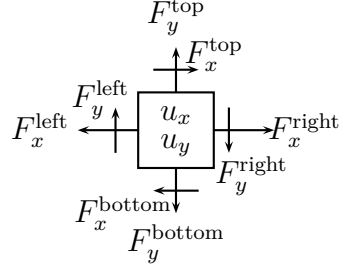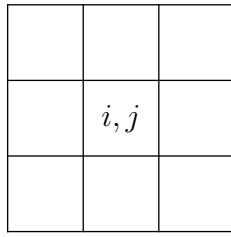
Figure 7: A cellular automata modeling approach considers a material divided into cells. The cell (i, j) interacts with its neighbors around, by applying forces on its faces.

i.e., square, rectangle, triangle and others. Thus, as finite elements, it is possible to mesh a complex material geometry as those found in industry.

On Fig. 8 the algorithm is presented for each step of computation. An excitation generates a stress or a displacement, in the material. Using Newton's second law it is possible to compute the acceleration of a particle in the material. Because time is discretized, speed can be derived from the acceleration. If Δt is a step of time, F forces per unit of volume, v_k speed (discretized with respect to time), ρ mass per unit of volume and a the acceleration, we have,

$$a = \frac{v_{k+1} - v_k}{\Delta t} = \frac{\sum F}{\rho}. \tag{49}$$

The displacement, u_k , is deduced from the speed, v_k , using again the time discretization. Eventually it is possible to compute the new Forces/Stress using Hooke's law.

3.1.2 Time and geometric resolution

The previous chapter showed that wave propagation is a robust tool among techniques used in SHM. It is important to know this point because it will condition parameters for CA simulations. Thus, this sections examines simulation preparation of wave propagation in a material depicted on Fig. 9. The case is idealized for a transverse wave, in order to focus on the method, and thus may not be real. The propagation is assumed to occur along the $x-$axis.

20
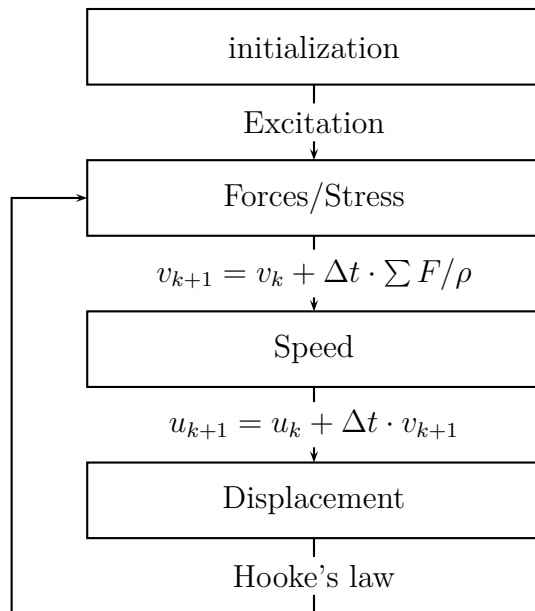
Figure 8: Loop in the CA algorithm. Each step involves interactions between a cell and its neighboring cells.
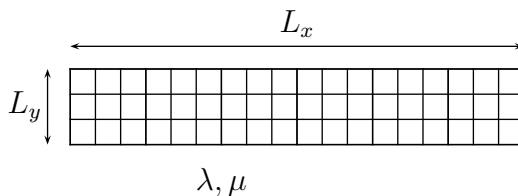
Figure 9: Rectangular material divided into square cells. The material is charaterized by the Lamé coefficients and its dimensions $L_x \times L_y$.

Before any simulations different parameters must be adapted to the physical phenomenon studied. For instance, if wave propagates at a frequency $f = 2\text{MHz}$, the sampling frequency $f_{\text{sampling}} = 10\text{MHz}$ gives a good time resolution. The least sampling frequency is driven by Nyquist's sampling theorem, but it is not high enough to watch a signal. This is the reason why the sampling frequency is bigger. Choosing the sampling frequency corresponds to choose the time step defined by $\Delta t = 1/f_{\text{sampling}}$. Later, the time step is chosen with some strict criterion. Therefore one should note that it is important to use the CA code with correct parameters, striking a compromise between accuracy and duration of the simulation.
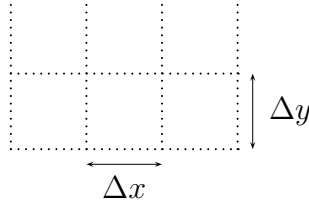
Figure 10: Detailed geometry

The lengths (L_x, L_y) of the material are divided into cells such that $\exists (N_x, N_y) \in \mathbb{N}^2 \mid L_x = N_x \Delta x$ and $L_y = N_y \Delta y$, as depicted on Fig. 9. For simplicity and only in this paragraph $\Delta x = \Delta y$. In order to have a good spatial resolution $10\Delta x = \lambda_{\text{wave}}$ is taken. Here λ_{wave} is the wave length and should not be confused with the Lamé coefficients λ and μ. The wave propagating along the $x-$axis is assumed to have the speed is $c_T = \sqrt{\mu/\rho}$. From the fundamental relation,

$$\lambda_{\text{wave}} = \frac{c_T}{f}, \tag{50}$$

it comes the two parameters Δx and N_x,

$$\Delta x = \frac{\sqrt{\mu/\rho}}{10f}, \tag{51}$$

$$N_x = \left\lfloor \frac{L_x}{\Delta x} \right\rfloor. \tag{52}$$

In the example the material is a thin aluminum plate with the proprieties stated in table 1. Eq. 52 and table 1 yield $N_x = 322$ and $\Delta x = 0.0015$ m for the spatial

Table 1: Wave traveling in an aluminum plate.

Physical quantities	Units	Values
ρ	kg.m^{-3}	2700
μ	Pa	$2.59 \ 10^{10}$
L_x	cm	5
L_y	mm	1
f	MHz	2

resolution. This example has shown the resolution parameters strongly depends on

the physics that needs to be observed. This step towards the simulation is important because it may radically change the numerical accuracy of results.

3.2 Stability of the code

This section will prove the stability of the code and give some hints on the convergence of the CA code. The method to prove the stability requires the von Neumann analysis. This method is a classic for proving stability in finite difference. In order to use such a method, Leamy provides in [3] the correspondence between CA and finite difference.

Because the finite difference method relies on the continuous equations, it is necessary to form the general equations of propagation in solid material. In three dimensions, the second Newton's law is defined by,

$$\underline{\text{div}}\ \underline{\underline{\sigma}} + \underline{f}^{\text{external}} = \rho\underline{\gamma}. \tag{53}$$

In two dimensions and without external forcing this law is given by,

$$\rho\frac{\partial^2 u_x}{\partial t^2} = \frac{\partial \sigma_{xx}}{\partial x} + \frac{\partial \sigma_{xy}}{\partial y}, \tag{54}$$

$$\rho\frac{\partial^2 u_y}{\partial t^2} = \frac{\partial \sigma_{yy}}{\partial y} + \frac{\partial \sigma_{xy}}{\partial x}. \tag{55}$$

u_x is the component on the $x-$axis and u_y is the component on the $y-$axis. σ is related to the displacement using linear Hooke's law,

$$\begin{pmatrix} \sigma_{xx} \\ \sigma_{yy} \\ \sigma_{xy} \end{pmatrix} = \begin{pmatrix} \lambda + 2\mu & \lambda & 0 \\ \lambda & \lambda + 2\mu & 0 \\ 0 & 0 & 2\mu \end{pmatrix} \begin{pmatrix} \varepsilon_{xx} \\ \varepsilon_{yy} \\ \varepsilon_{xy} \end{pmatrix}. \tag{56}$$

From that point, the strain $\underline{\underline{\varepsilon}}$ is related two the displacement $\underline{u}$ by the compatibility equation,

$$\underline{\underline{\varepsilon}} = \frac{1}{2}\left(\underline{\underline{\nabla}}\,\underline{u} + \underline{\underline{\nabla}}^{\text{T}}\underline{u}\right), \tag{57}$$

then,

$$
\begin{pmatrix} \varepsilon_{xx} \\ \varepsilon_{yy} \\ \varepsilon_{xy} \end{pmatrix} = \begin{pmatrix} u_{x,x} \\ u_{y,y} \\ (1/2)(u_{x,y} + u_{y,x}) \end{pmatrix}.
\tag{58}
$$

$_{,x}$ denotes the derivative with respect to x. To form the final PDE, Eq. 58 is plugged back into Eq. 56 and then plugged back into Eq. 54 and 55. Eventually, two equations with two unknown functions (u_x, u_y) can be formed.

$$
\rho \frac{\partial^2 u_x}{\partial t^2} = (\lambda + 2\mu)\frac{\partial^2 u_x}{\partial x^2} + (\lambda + \mu)\frac{\partial^2 u_y}{\partial x \partial y} + \mu \frac{\partial^2 u_x}{\partial y^2}
\tag{59}
$$

$$
\rho \frac{\partial^2 u_y}{\partial t^2} = (\lambda + 2\mu)\frac{\partial^2 u_y}{\partial y^2} + (\lambda + \mu)\frac{\partial^2 u_x}{\partial x \partial y} + \mu \frac{\partial^2 u_y}{\partial x^2}
\tag{60}
$$

These two equation are wave equations. Indeed there are two time derivatives with respect to time, t on the left hand side and two derivatives with respect to space variables (x, y) on the right hand side. Resolution by hand is explored in later chapters.

3.2.1 Discretization

A point is localized in time and space with new variable. Previously $(x, y, t) \in \mathbb{R}^3$ specified the coordinates of a particular point, with constraints on (x, y) to be in the material domain. Now, points are located with the variables $(i, j, k) \in \mathbb{N}^3$. x (resp. y, t) corresponds to i (resp. j, k).

For functions such as the displacement it comes $u_y(i\Delta x, j\Delta y, k\Delta t) = {}_y u_{i,j}^k$ highlights the correspondence. Discretization also affects the derivative, centered scheme are used as an approximation. This leads to,

$$
\frac{\partial^2 u_y}{\partial y^2}(x, y, t) \approx \frac{{}_y u_{i,j+1}^k - 2 {}_y u_{i,j}^k + {}_y u_{i,j-1}^k}{\Delta y^2}.
\tag{61}
$$

To emphasize the adjective "centered" the reader may refer to the sketch on figure 11.

Proceeding the same way Eq. 59 and 60, it could be written as the following

24
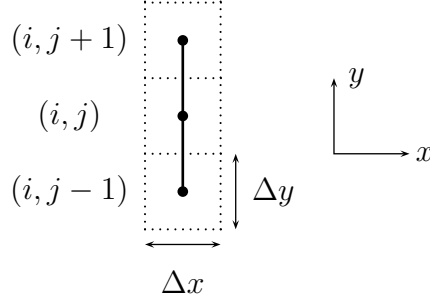
Figure 11: Centered scheme for $u_{y,yy}$

system of Eq. 62 and 63,

$$
\begin{cases}
{}_y v_{i,j}^{k+1} = {}_y v_{i,j}^{k} \\
\qquad + \frac{\Delta t}{\Delta y^2} \frac{\lambda+2\mu}{\rho} \left({}_y u_{i,j+1}^{k} - 2\,{}_y u_{i,j}^{k} + {}_y u_{i,j-1}^{k} \right) \\
\qquad + \frac{\Delta t}{4\Delta y \Delta x} \frac{\lambda+\mu}{\rho} \left({}_x u_{i+1,j+1}^{k} - {}_x u_{i-1,j+1}^{k} + {}_x u_{i-1,j-1}^{k} - {}_x u_{i+1,j-1}^{k} \right) \quad (62) \\
\qquad + \frac{\Delta t}{\Delta y^2} \frac{\mu}{\rho} \left({}_y u_{i+1,j}^{k} - 2\,{}_y u_{i,j}^{k} + {}_y u_{i-1,j}^{k} \right) \\
{}_y u_{i,j}^{k+1} - \Delta t\,{}_y v_{i,j}^{k+1} = {}_y u_{i,j}^{k}
\end{cases}
$$

and,

$$
\begin{cases}
{}_x v_{i,j}^{k+1} = {}_x v_{i,j}^{k} \\
\qquad + \frac{\Delta t}{\Delta x^2} \frac{\lambda+2\mu}{\rho} \left({}_x u_{i,j+1}^{k} - 2\,{}_x u_{i,j}^{k} + {}_x u_{i,j-1}^{k} \right) \\
\qquad + \frac{\Delta t}{4\Delta y \Delta x} \frac{\lambda+\mu}{\rho} \left({}_y u_{i+1,j+1}^{k} - {}_y u_{i-1,j+1}^{k} + {}_y u_{i-1,j-1}^{k} - {}_y u_{i+1,j-1}^{k} \right) \quad (63) \\
\qquad + \frac{\Delta t}{\Delta x^2} \frac{\mu}{\rho} \left({}_x u_{i+1,j}^{k} - 2\,{}_x u_{i,j}^{k} + {}_x u_{i-1,j}^{k} \right) \\
{}_x u_{i,j}^{k+1} - \Delta t\,{}_x v_{i,j}^{k+1} = {}_x u_{i,j}^{k}.
\end{cases}
$$

The systems are presented such that, $k + 1$ subscripts are on the left side while k subscripts are the right side. This separation has the advantage of emphasizing each step of the algorithm.

Lemma 3.2.1 (Leamy). *The CA algorithm considers the discretized systems 62 and 63.*

Proof. In [3], Leamy first computes the speed and then the displacement,

$$\frac{\partial v_y}{\partial t}(x, y, t) \approx \frac{{}_y v_{i,j}^{k+1} - {}_y v_{i,j}^k}{\Delta t} \tag{64}$$

and,

$${}_y v_{i,j}^{k+1} = \frac{{}_y u_{i,j}^{k+1} - {}_y v_{i,j}^k}{\Delta t}. \tag{65}$$

Thus by combining the last two equations gives the second order differential,

$$\frac{\partial^2 u_y}{\partial t^2}(x, y, t) \approx \frac{{}_y u_{i,j}^{k+1} - 2\,{}_y u_{i,j}^k + {}_y u_{i,j}^{k-1}}{\Delta t^2}. \tag{66}$$

Any other equations follow this discretization process and at the end will yield Eq. 62 and 63 $\qquad\square$

This separation for Eq. 64 and Eq. 65, i.e. speed then displacement, is more efficient than writing directly Eq. 66, because for stability consideration is better to manipulate only k and $k + 1$. This lemma proves the correspondence between CA and finite difference. And immediate consequence is the possibility to use classical tools for stability analysis.

3.2.2 Stability : von Neumann analysis

In this subsection stability of the CA code is proved using von Neumman analysis.

Definition 3.2.2 (Stability). A finite one-step difference scheme $P_{\Delta t, \Delta x, \Delta y} u_{i,j}^k = 0$ for a first order PDE is stable if there exist for any time $T \geq 0$, there exist numbers $\Delta x_0 > 0$, $\Delta y_0 > 0$ and $\Delta t_0 > 0$ such that for any $T > 0$ there exists a constant C_T such that

$$\|u_{i,j}^k\| \leq C_T \|u_{i,j}^0\|$$

for $0 \leq k\Delta t \leq T$, $0 < i\Delta x \leq \Delta x_0$, $0 < j\Delta y \leq \Delta y_0$, $0 < k\Delta t \leq \Delta t_0$.

To analyze the stability it is preferable, to start with a simpler example. The 1D wave equation is,

$$\frac{\partial^2 u}{\partial t^2} - c^2 \frac{\partial^2 u}{\partial x^2} = 0. \tag{67}$$

An intermediate variable is introduced, the speed v, to form a system of equations that has only on derivation with respect to time.

$$\begin{cases} \partial v/\partial t & = c^2 (\partial^2 u)/(\partial x^2) \\ (\partial u)/(\partial t) & = v \end{cases} \tag{68}$$

The discretized corresponding system is,

$$\begin{cases} v_m^{k+1} & = v_m^k + c^2 \frac{\Delta t}{\Delta x^2} \left(u_{m+1}^k - 2u_m^k + u_{m-1}^k \right), \\ u_m^{k+1} - \Delta t \, v_m^{k+1} & = u_m^k. \end{cases} \tag{69}$$

Now the discrete Fourier transform of the system will allow us to get rid of the spatial subscript m. By the Parseval theorem the norms are equal in Fourier space and the original space. Thus, stability can be proved in any space thanks to the isometry.

Definition 3.2.3 (Discrete Fourier Transform). f is defined as its collection of values on the grid $f = (..., f_{-1}, f_0, f_{-1}, ...)$ with the space between two consecutive points, Δx

$$\forall \xi \in [-\pi/\Delta x, \pi/\Delta x] \qquad \hat{f}(\xi) = \frac{1}{\sqrt{2\pi}} \sum_{m=-\infty}^{\infty} e^{-im\Delta x \xi} f_m \Delta x$$

$$f_m = \frac{1}{\sqrt{2\pi}} \int_{-\pi/\Delta x}^{\pi/\Delta x} e^{im\Delta x} \hat{f}(\xi) d\xi.$$

Theorem 3.2.4. *The scheme 69 is stable under the CFL condition.*

Proof. Using the Fourier inversion formula on the speed,

$$v_m^k = \frac{1}{\sqrt{2\pi}} \int_{-\pi/\Delta x}^{\pi/\Delta x} e^{im\Delta x} \hat{v}^k(\xi) d\xi.$$

Using the same procedure on Eq. 69, the system becomes,

$$\frac{1}{\sqrt{2\pi}} \int_{-\pi/\Delta x}^{\pi/\Delta x} e^{im\Delta x} \hat{v}^{k+1}(\xi) d\xi = \frac{1}{\sqrt{2\pi}} \int_{-\pi/\Delta x}^{\pi/\Delta x} e^{im\Delta x} \hat{v}^k(\xi) + [R(2\cos(\Delta x\ \xi) - 2)]\hat{u}^k(\xi) d\xi,$$

(70)

where $(R = c^2 \Delta t/\Delta x^2)$. Because Discrete Fourier Transform is unique,

$$\hat{v}^{k+1}(\xi) = \hat{v}^k(\xi) + [R(2\cos(\Delta x\ \xi) - 2)]\hat{u}^k(\xi),$$

(71)

and,

$$\hat{u}^{k+1}(\xi) - \Delta t\ \hat{v}^{k+1}(\xi) = \hat{u}^k(\xi).$$

(72)

The system is linear thus matrix formalism leads to $(\beta = \Delta x\ \xi)$,

$$\begin{pmatrix} 0 & 1 \\ 1 & -\Delta t \end{pmatrix} \begin{pmatrix} \hat{u}^{k+1} \\ \hat{v}^{k+1} \end{pmatrix} = \begin{pmatrix} -4R\sin^2(\beta/2) & 1 \\ 1 & 0 \end{pmatrix} \begin{pmatrix} \hat{u}^k \\ \hat{v}^k \end{pmatrix}$$

(73)

The vector w is formed as $w = (u, v)$. The numerical scheme is stable if $\|\hat{w}^n\| = \|w^n\| \le \|w^0\|$. In other words, the matrix

$$\begin{pmatrix} 0 & 1 \\ 1 & -\Delta t \end{pmatrix}^{-1} \begin{pmatrix} -4R\sin^2(\beta/2) & 1 \\ 1 & 0 \end{pmatrix} = \begin{pmatrix} 4R\Delta t\sin^2(\beta/2) + 1 & -\Delta t \\ -4R\sin^2(\beta/2) & 1 \end{pmatrix}$$

(74)

has all its eigenvalues smaller or equal to 1 in terms of modulus. The characteristic polynomial χ is,

$$\chi(X) = X^2 + [-4\Delta t R\sin^2(\beta/2) + 2]X + 1.$$

(75)

If λ_1 and λ_2 are the two eigenvalues there is $|\lambda_1| \cdot |\lambda_2| = 1$. The eigenvalues must be on the unit circle to verify the stability. This implies that they must have the same modulus because only complex roots verify this point. This yields discriminant Δ to be smaller than zero,

$$\Delta = (-4\Delta t R\sin^2(\beta/2) + 2)^2 - 4$$

$$= (-4\Delta t R\sin^2(\beta/2))^2 + 4(-4\Delta t R\sin^2(\beta/2)) \le 0,$$

(76)

28

giving,

$$4\Delta t R \sin^2(\beta/2) \leq 4$$

$$\Delta t R \leq 1$$

$$\left| c\frac{\Delta t}{\Delta x} \right| \leq 1. \tag{77}$$

$\square$

Remark 3.2.5 (Numerical verification). The CFL (Courant-Friedrichs-Lewy) condition gives stability to the scheme. MATLAB simulation is performed for $\Delta t = \Delta x/(\alpha.c)$ with different values of the parameter α. It computes,

$$\max_{0\leq\beta\leq2\pi} |\text{eig}(D)| , \tag{78}$$

$$\text{where } D = \begin{pmatrix} 4R\Delta t \sin^2(\beta/2) - 1 & -\Delta t \\ 4R\sin^2(\beta/2) & -1 \end{pmatrix}.$$

Table 2 contains simulation results. It is easy to conclude that under the CFL condition, the scheme is stable. This assertion has been verified theoretically and numerically.

Table 2: Results of simulation for different values of the parameter α.

α	max eigenvalues
0.1	397.8245
0.8	3.9971
0.9	2.5429
1	1
2	1
3	1

3.2.2.2   Back to the 2D problem

From this point the original scheme 62 and 63 is considered. The same strategy is applied here. First, we use some notations,

$$\hat{w}^k = (_x\hat{u}^k,\, _y\hat{u}^k,\, _x\hat{v}^k,\, _y\hat{v}^k),$$

$$r_1^y = \frac{\Delta t}{\Delta y^2}\frac{\lambda+2\mu}{\rho},$$

$$r_1^x = \frac{\Delta t}{\Delta x^2}\frac{\lambda+2\mu}{\rho},$$

$$r_2 = \frac{\Delta t}{\Delta x \Delta y}\frac{\lambda+\mu}{4\rho},$$

$$r_3^y = \frac{\Delta t}{\Delta y^2}\frac{\mu}{\rho},$$

$$r_3^x = \frac{\Delta t}{\Delta x^2}\frac{\mu}{\rho},$$

$$\beta_x = k_i\Delta x,$$

$$\beta_y = k_j\Delta y.$$

After using the same procedure as before (reducing the degree of derivation on the left and apply the Discrete Fourier Transform), it becomes,

$$\begin{pmatrix} 1 & 0 & -\Delta t & 0 \\ 0 & 1 & 0 & -\Delta t \\ 0 & 0 & 1 & 0 \\ 0 & 0 & 0 & 1 \end{pmatrix} \begin{pmatrix} _x\hat{u}^{k+1} \\ _y\hat{u}^{k+1} \\ _x\hat{v}^{k+1} \\ _y\hat{v}^{k+1} \end{pmatrix} =$$

$$\begin{pmatrix} 1 & 0 & 0 & 0 \\ 0 & 1 & 0 & 0 \\ -4r_2\sin\beta_x\sin\beta_y & -4(r_1^y\sin^2(\beta_y/2)+r_3^x\sin^2(\beta_x/2)) & 1 & 0 \\ -4(r_1^x\sin^2(\beta_x/2)+r_3^y\sin^2(\beta_y/2)) & -4r_2\sin\beta_x\sin\beta_y & 0 & 1 \end{pmatrix} \begin{pmatrix} _x\hat{u}^k \\ _y\hat{u}^k \\ _x\hat{v}^k \\ _y\hat{v}^k \end{pmatrix},$$

$$(79)$$

or more simply,

$$A\hat{w}^{k+1} = B\hat{w}^k. \tag{80}$$

The previous example showed that the discrete scheme is stable if the eigenvalues of $A^{-1}B$ are smaller than 1. Here it looks difficult to formulate an inequality like in the example. Thus use of simulation gives intuition on the eigenvalues.

The spatial resolution Δx and Δy are determined by the Eq. 51. The time step Δt is computed with respect to stability consideration. Again using the celerity of the P-wave and assuming that the system verifies the the CFL condition, it will verifies

the CFL for all the other waves,

$$\text{If for } \Delta t \leq \frac{\Delta x}{c_P}, \text{ then } \forall c \leq c_P \Rightarrow \Delta t \leq \frac{\Delta x}{c}.$$

Again a MATLAB simulation is performed for different values of the parameter α in $\Delta t = \Delta x / \alpha c_P$. It computes,

$$\max_{0 \leq \beta_x \leq 2\pi} \max_{0 \leq \beta_y \leq 2\pi} \left| \text{eig}(A^{-1}B) \right|. \tag{81}$$

For different values of the parameter α, the eigenvalues of $A^{-1}B$ are hoped to be smaller than 1. Results are presented in table 3. It shows that the biggest eigenvalue

Table 3: Results of simulation.

α	max eigenvalues
0.1	502.8087
0.8	9.7223
0.9	8.0588
1	6.8624
10	1.2502
20	1.1183
100	1.0226
1000	1.0022
10000	1.0002

never reach the value 1, as in the previous section. Thus the proof will require more work than previously because a sharper criterion must be found if it exists.

Definition 3.2.6 (Spectral radius)**.** Spectral radius consists in the biggest eigenvalue in modulus.

$$\lambda_{\max} = \max \left| \text{eig}(A^{-1}B) \right| \tag{82}$$

Remark 3.2.7. Before continuing, it is easier to consider space of eigenvectors. Q is the matrix that allows us to change the basis, defined as $A^{-1}B = Q\Xi Q^{-1}$, where Ξ is the diagonal matrix with the eigenvalues. In this new basis

$$Q^{-1}\hat{w}^{k+1} = \Xi Q^{-1}\hat{w}^k. \tag{83}$$

Lemma 3.2.8. *If P is an invertible matrix, p_k are the n eigenvectors of the symmetric matrix P^*P, and μ_k are the n eigenvalues of the symmetric matrix P^*P. Then,*

$$\exists A, B > 0 \quad \forall f \quad A\|f\| \le \|Pf\| \le B\|f\|$$

Proof.

$$\|Pf\|^2 = \langle Pf, Pf \rangle \tag{84}$$

$$= \langle f, P^*Pf \rangle \tag{85}$$

$$= \sum_{k=1}^{n} \mu_k \langle p_k, f \rangle^2 \quad \text{Parseval: decomposition on the } p_k \perp\text{-basis} \tag{86}$$

$A = \min_k \mu_k$ and $B = \max_k \mu_k$ give the answer. $A \ne 0$ because P is invertible. $\qquad \square$

Remark 3.2.9. If P is symmetric then $A = B = 1$.

Proposition 3.2.10.

$$\exists c > 0, \quad \|\hat{w}^k\| \le c\lambda_{\max}^k \|\hat{w}^0\|.$$

Proof. Starting from equation 83

$$Q^{-1}\hat{w}^{k+1} = \Xi Q^{-1}\hat{w}^k \tag{87}$$

$$Q^{-1}\hat{w}^k = \Xi^k Q^{-1}\hat{w}^0. \tag{88}$$

With the squared norm we have it comes,

$$\|Q^{-1}\hat{w}^k\|^2 = \sum_i \lambda_i^{2k}(Q^{-1}\hat{w}^0)_i^2 \tag{89}$$

$$\|Q^{-1}\hat{w}^k\|^2 \le \lambda_{\max}^{2k} \sum_i (Q^{-1}\hat{w}^0)_i^2 \tag{90}$$

$$\|Q^{-1}\hat{w}^k\| \le \lambda_{\max}^k \|Q^{-1}\hat{w}^0\|. \tag{91}$$

With the previous lemma, $a = \min \; \mathrm{eig}\{Q^{-1*}Q^{-1}\}$ and $b = \max \; \mathrm{eig}\{Q^{-1*}Q^{-1}\}$,

$$a\|\hat{w}^k\| \le \|Q^{-1}\hat{w}^k\| \le \lambda_{\max}^k\|Q^{-1}\hat{w}^0\| \le b\lambda_{\max}^k\|\hat{w}^0\|, \tag{92}$$

$a \ne 0$ because Q^{-1} is invertible. To complete the proof $c = b/a$ is chosen. $\qquad\square$

Proposition 3.2.11.

$$\exists K > 0, \quad \lambda_{\max} < 1 + K\Delta t$$

Proof. The proposition is assumed to be true given the numerical results of Tab. 3. $\quad\square$

Theorem 3.2.12. *The scheme described by the Eq. 62 and 63 is stable.*

Proof. With the proposition 3.2.10 it comes,

$$\exists c > 0 \quad \|\hat{w}^k\| \le c\lambda_{\max}^k\|\hat{w}^0\|. \tag{93}$$

If we use the proposition 3.2.11 we have

$$\exists c, K > 0 \quad \|\hat{w}^k\| \le c(1 + K\Delta t)^k\|\hat{w}^0\|. \tag{94}$$

For a fixed a time T the $\forall k$ s.t. $k\Delta t \le T$

$$\|\hat{w}^k\| \le c(1 + K\Delta t)^{T/\Delta t}\|\hat{w}^0\|$$

$$\|\hat{w}^k\| \le c\, e^{KT}\|\hat{w}^0\|$$

$$\|\hat{w}^k\| \le C_T\|\hat{w}^0\|.$$

Because the Fourier transform is an isometry.

$$\|w^k\| \le C_T\|w^0\| \tag{95}$$

This ends the proof of stability. $\qquad\square$

Remark 3.2.13. At the beginning of the chapter there was $\Delta t = 1/f_{\text{sampling}}$ to have a good time resolution. From table 3, $\Delta t \le \Delta x/(10\ c_P)$ is the other consideration for a nice spatial resolution $\lambda_{\max} \approx 1$. These considerations lead to the time criterion

$$\Delta t = \min\left(\frac{1}{f_{\text{sampling}}}, \frac{\Delta x}{10\ c_P}\right). \tag{96}$$

3.2.3 Consistency and convergence

Definition 3.2.14 (Consistency)**.** A finite difference scheme $P_{\Delta t, \Delta x, \Delta y} u_{i,j}^k = 0$ is consistent with the PDE $Pu = 0$ of order (q, r, s) if for any smooth function ϕ

$$P\phi - P_{\Delta t, \Delta x, \Delta y}\phi = O(\Delta t^q, \Delta x^r, \Delta y^s).$$

Consistency is very easy to verify using Taylor series. From the Eq. 66, it comes,

$$\forall \phi \text{ smooth} \qquad P_{\Delta t, \Delta x, \Delta y}\phi = \frac{\phi_{i,j}^{k+1} - 2\phi_{i,j}^k + \phi_{i,j}^{k-1}}{\Delta t^2}$$
$$= \frac{\phi(t + \Delta t, x, y) - 2\phi(t, x, y) + \phi(t - \Delta t, x, y)}{\Delta t^2}$$

Then the Taylor series implies the following expansion

$$P_{\Delta t, \Delta x, \Delta y}\phi = \frac{\partial^2 \phi}{\partial t^2} + O(\Delta t)$$
$$= P\phi + O(\Delta t). \tag{97}$$

Lemma 3.2.15. *The scheme 62 and 63 is consistent.*

Proof. Proceeding the same way (paragraph above) on the system 62 and 63 it is trivial to see that the scheme is consistent. $\qquad\square$

Definition 3.2.16 (well-posed problem)**.** A problem is said to be well-posed if for the first order PDE $Pu = 0$ if for any time $T \geq 0$, there is a constant C_T, such that any solution $u(x, t)$ satisfies

$$\|u(t, x)\| = C_T \|u(0, x)\|.$$

Remark 3.2.17. This means that the solution is of continuous dependency for its initial conditions.

The mechanical problem of the waves in a plate is assumed to be well-posed. The proof of such a propriety relies on the boundary conditions and distribution theory. Some hints are given here to suggest the proof. Indeed the boundary condition are well
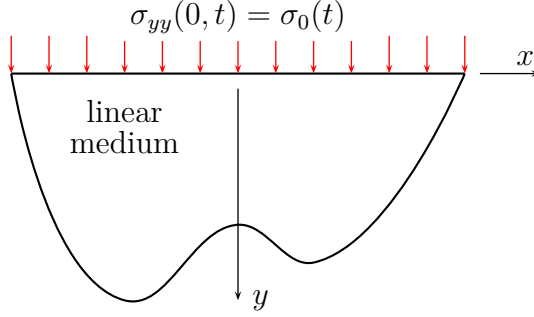
Figure 12: Semi infinite and linear medium submitted to an external forcing $\sigma_0(t)$ on the whole surface.

defined. Indeed if the boundary of the plate is noted $\partial\Omega$, the stress boundary Γ_C and the boundary with displacement condition Γ_D. In the problem there is $\partial\Omega = \Gamma_C \cup \Gamma_D$ and $\Gamma_C \cap \Gamma_D = \{\emptyset\}$.

Definition 3.2.18 (Convergence). A discrete scheme $P_{\Delta t, \Delta x, \Delta y} u_{i,j}^k = 0$ is convergent if $u_{i,j}^k$ converge to the continuous solution u as $\Delta t \to 0$, $\Delta x \to 0$ and $\Delta y \to 0$.

Theorem 3.2.19 (Lax). *A consistent finite difference scheme for PDE for which the initial value problem is well-posed, is convergent if and only if it is stable.*

It gives the convergence for the scheme. Practically the finer is the spatial resolution and the time step the smaller will be the error. In other words accuracy only requires small Δt, Δx and Δy.

3.3 Accuracy in practise

In this section a numerical solution is compared to an analytical solution for a linear material with semi-infinite dimensions.

3.3.1 Solution for the linear 1-D problem

A semi-infinite medium is excited on its upper boundary, as presented on the Fig. 12. This gives a nice perspective to study the analytical problem, because the local displacement of the material particles can be assumed only with respect to $y-$axis and
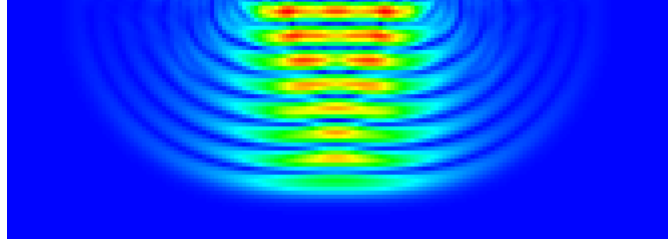
Figure 13: Numerical simulation, approximation of a plane wave

depends on y. This leads to,

$$\begin{pmatrix} u_x(x,y,t) \\ u_y(x,y,t) \end{pmatrix} = \begin{pmatrix} 0 \\ u_y(y,t) \end{pmatrix} \tag{98}$$

For reasons of simplicity the subscript y is omitted and thus $u_y(\cdot) = u(\cdot)$. In this problem the wave equation is,

$$\frac{\partial^2 u}{\partial t^2} = \frac{\lambda + 2\mu}{\rho} \frac{\partial^2 u}{\partial y^2} \tag{99}$$

The celerity of the wave is, $c_P^2 = (\lambda + 2\mu)/\rho$. However in the code and as presented on the Fig. 12 the boundary condition at $y = 0$ is given for the stress. It is easy to show that the stress σ_{yy} verifies the same wave Eq. 99. The analytical solution for the model is given by

$$\sigma_{yy}(y,t) = \sigma_0(t - y/c). \tag{100}$$

Practically, the surface is excited the surface of the plate on an area L much bigger than the wave-length. All assumptions are explained in details in the next chapter. Here it is assumed that the excitation is equivalent to an excitation on the infinite top surface of the plate. On Fig. 13, it is remarkable that the plane wave assumption is verified only close to the external forcing.

3.3.2 Test for a sine

The excitation on top F_{external} is a sine at the single frequency f_0,

$$F_{\text{external}}(t) = F_0 \sin(2\pi f_0(t)) \tag{101}$$

36

The stress σ_0 is related to F_{external} by the width w (the $z-$axis) and the length Δx of the cell,

$$\sigma_0(t) = -\frac{F_{\text{external}}(t)}{w \, \Delta x}.$$ (102)

The parameters for the excitation on the top of the plate are stated in table 4.

Table 4: External forcing parameters.

Quantities	Units	Values
F_0	N	100
f_0	MHz	5.0

The data is collected at one point M. Then a comparison between the numerical result and the theoretical case is performed. The geometrical properties for the numerical experiment are stated below.

Table 5: Geometrical proprieties and CA code parameters.

Physical quantities	Units	Values
L_x	cm	2
L_y	cm	1
Δx	m	10^{-4}
Δy	m	10^{-4}
L	cm	1
x_m	m	0
y_m	m	$5 \; 10^{-4}$

The theoretical solutions can be derived using Eq. 100,

$$\sigma(y, t) = -\frac{F_0}{w \, \Delta x} \sin(2\pi f_0(t - y/c_P)),$$ (103)

or, in terms of displacement

$$u(y, t) = \frac{F_0}{w \, \Delta x} \frac{1}{k(\lambda + 2\mu)} (1 - \cos(\omega t - ky)).$$ (104)

In order to measure the accuracy of the code the squared error of simulation SE is introduced , as a positive scalar. If f is the exact solution and $\tilde{f}$ is the numerical

37
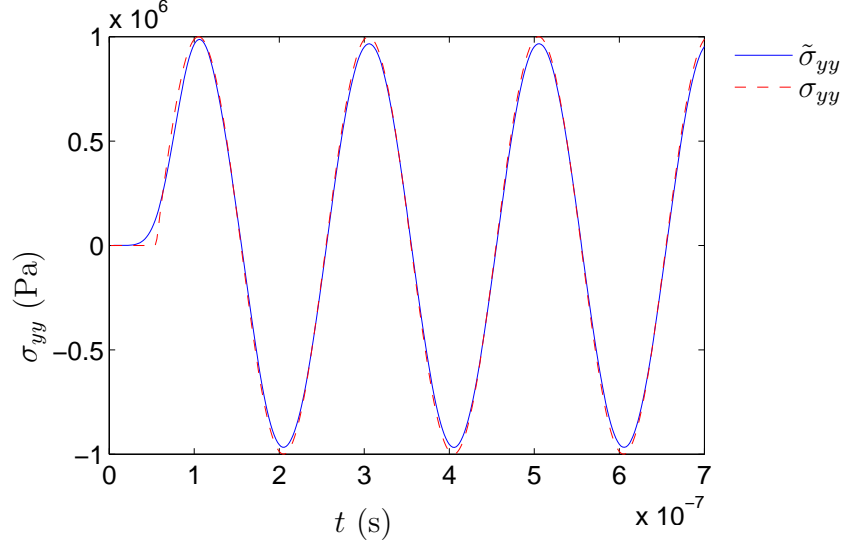
Figure 14: Simulation for the stress σ_{yy} in a linear material

solution, then

$$SE : L_2(\mathbb{R}) \longmapsto \mathbb{R}_+ \tag{105}$$

$$SE : f \longrightarrow \sqrt{\frac{\int_{\mathbb{R}} (f - \tilde{f})^2 dt}{\int_{\mathbb{R}} f^2 dt}} = \frac{\|f - \tilde{f}\|_2}{\|f\|_2}. \tag{106}$$

Fig. 14 depicts the accuracy of the code is explored in terms of the stress σ_{yy}. The $SE(\sigma_{yy})$ equals 4.6%. The result is quite good but not as accurate as for the displacement u_y. Indeed the code gives $SE(u_y) = 1.2\%$. The two results are parts of a unique simulation i.e. the stress and the displacement were written during one compution.

It can be concluded that the code solves the displacement better than the stress. The stress σ is just an intermediate calculation computed using the derivative of u. This operation always yields losses in precision (contrary to integration) which result in a worse but not bad SE.

Figure 15: Simulation for the displacement u_y in a linear material

CHAPTER IV

P-WAVE IN A NON-LINEAR MATERIAL

After studying the theory and understanding the CA code, the non-linear Hooke's law is implemented. The new algorithm is depicted on Fig. 16. Quadratic terms are added to the constitutive law for the cells inside the material. This set of rule establishes interaction with a cell and its neighbors. However the 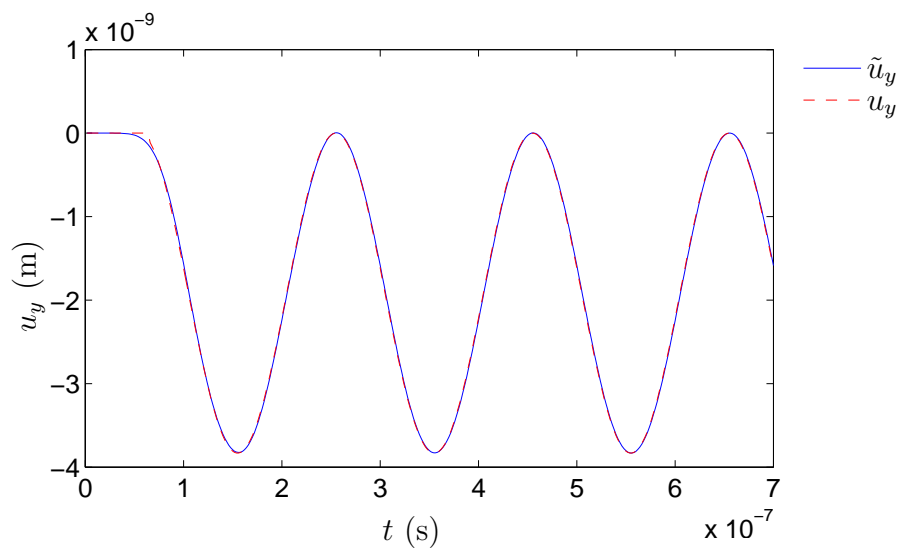cells on the free stress boundaries requires additional work because the interactions rules are different and should include non-linearities.

At the moment there exist no proof for stability and convergence for a non-linear scheme. However accuracy of the new code must be validated with a comparison between closed form solution and computational solution

4.1   Numerical computation of the free stress boundary condition

The computation of the displacement on the boundaries requires to write equilibrium on the free surface,

$$\underline{\underline{\sigma}}(\Gamma_C) \cdot \underline{n} = \underline{0}, \tag{107}$$

where $\underline{n}$ is the vector normal to the surface. A rectangle geometry depicted on Fig. 18 is still considered for the material geometry. Thus the normal vector will be either $\underline{n} = \pm\underline{e}_x$, for the left or right side, or $\underline{n} = \pm\underline{e}_y$ for the top or bottom side. For instance the top free surface problem to solve is,

$$\begin{cases} \sigma_{yy}(y = 0) = 0 \\ \sigma_{xy}(y = 0) = 0 \end{cases} . \tag{108}$$

40
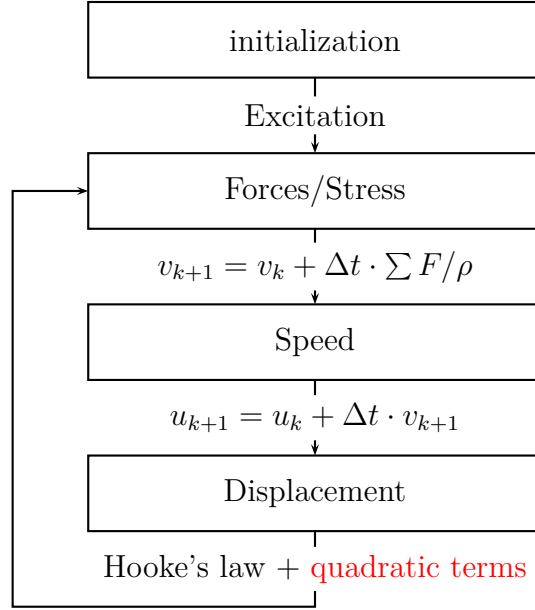
Figure 16: Algorithm for the non-linear problem
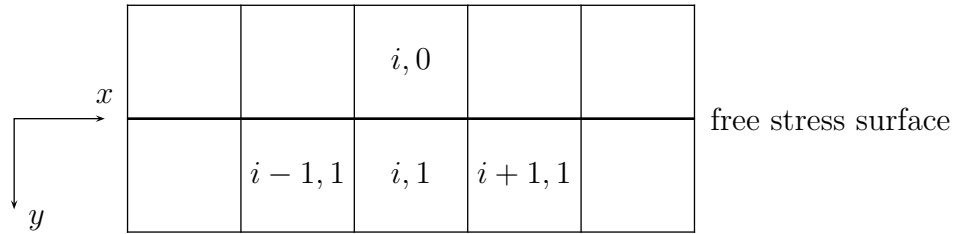
Figure 17: Top boundary of the material. The cells with the subscript $i, 0$ are above the the free surface, while the cells $i, 1$ belong to the inner domain.

4.1.1   Linear top free surface

Before solving the non-linear problem, the free surface problem is explored for a linear material, as in the article [3]. On Fig. 17 the cells with the subscript $(i, 0)$ do not belong to the material. Then these cells are called the ghost cells. The displacement and the stress of these cells are computed with rules such that, it will give a free stress boundary. The cells with the subscript $(i, 1)$ consist in the top layer cells.

In order to solve $_{0,i}u_x$ and $_{0,i}u_y$, it is necessary to write the stress computation for

cell $0, i$ on its bottom face,

$$\sigma_{yy}(y = 0) = \lambda\varepsilon_{xx} + (\lambda + 2\mu)\varepsilon_{yy} = 0 \tag{109}$$

$$\sigma_{xy}(y = 0) = 2\mu\varepsilon_{xy} = 0. \tag{110}$$

Remark 4.1.1. In the sense of continuous equations it is not correct to use the Hooke's law on the boundary because this equation is a field equation. However in the CA code the addition of an extra layer of cell allows to use that rule for displacement computation.

Then, these two Eq. 109 and 110 are written in the discrete domain, in terms of cells displacement. However the surface does not allow to compute the derivative like for the inner material. The centered derivation is sometime replaced by a shorter derivative.

$$\lambda\frac{_{1,i+1}u_x - _{1,i-1}u_x}{2\Delta x} + (\lambda + 2\mu)\frac{_{1,i}u_y - _{0,i}u_y}{\Delta y} = 0 \tag{111}$$

$$\mu\left(\frac{_{1,i}u_x - _{0,i}u_x}{\Delta y} + \frac{_{1,i+1}u_y - _{1,i-1}u_y}{2\Delta x}\right) = 0. \tag{112}$$

This linear system of two equations has two unknowns $_{0,i}u_x$ and $_{0,i}u_y$. The solutions are,

$$_{0,i}u_x = {}_{1,i}u_x + \frac{\Delta y}{2\Delta x}\left({}_{1,i+1}u_y - _{1,i-1}u_y\right) \tag{113}$$

$$_{0,i}u_y = {}_{1,i}u_y + \frac{\lambda\Delta y}{2\Delta x(\lambda + 2\mu)}\left({}_{1,i+1}u_x - _{1,i-1}u_x\right). \tag{114}$$

For the non-linear material this computation on the top layer cells takes into account quadratic terms.

4.1.2 Non-linear top free surface

For a non-linear material the stress condition, i.e. equilibrium condition, is the same but the Hooke's law is different,

$$\sigma_{yy}(y=0) = \lambda\varepsilon_{xx} + (\lambda+2\mu)\varepsilon_{yy} + \varepsilon_{xx}^2(B+C) + \varepsilon_{yy}^2(A+3B+C)$$

$$+ \varepsilon_{xy}^2(A+2B) + \varepsilon_{xx}\varepsilon_{yy}(2C+2B) = 0, \tag{115}$$

$$\sigma_{xy}(y=0) = 2\mu\varepsilon_{xy} + \varepsilon_{xx}\varepsilon_{xy}(2B+A) + \varepsilon_{yy}\varepsilon_{xy}(2B+A) = 0. \tag{116}$$

As seen before the two unknowns $_{0,i}u_x$ and $_{0,i}u_y$ are respectively contained in ε_{xy} and ε_{yy}, as it was shown in the above paragraph. Consequently the system of Eq. 115 and 116 is solved for the unknowns ε_{xy} and ε_{yy}, then $_{0,i}u_x$ and $_{0,i}u_y$ will immediately come. This change of variable has the aim to produce simpler equations.

The system to solve is non-linear because of the quadratic terms. Thus the uniqueness of the solution is not taken for granted. Each quadratic equation describes a conic section which is a curve obtained by intersecting a cone with a plane. If the two equation represent ellipses, their intersection can give none, one, two, three, four or an infinite number of solution.

The two equations yield four different solutions. The expression 116 can be written as,

$$\varepsilon_{xy}\left[2\mu + \varepsilon_{xx}(2B+A) + \varepsilon_{yy}(2B+A)\right] = 0 \tag{117}$$

Eq. 117 has two distinct solutions. Each solution injected in Eq. 115 yields two solutions. Thus there exist a total of four couple solution to this problem. However by using solution of the linear case it is easy to sort good or inaccurate solutions. With that aim, it is convenient to state the proposition 4.1.2.

Proposition 4.1.2. *The solution of the non-linear problem is required to be continuous with A, B and C at the point $(0,0,0)$.*

Corollary 4.1.3. *Consequently, if $A \to 0$, $B \to 0$ and $C \to 0$ the solution of the non-linear problem must converge to the solution of the linear problem.*

Proof. This corollary is the immediate consequence of continuity. □

By choosing from the Eq. 117, ε_{yy}, it comes

$$\varepsilon_{yy} = -\varepsilon_{xx} - \frac{2\mu}{2B + A}. \tag{118}$$

It is immediate to see that,

$$\lim_{A,B,C \to 0} \varepsilon_{yy} = \infty, \tag{119}$$

which contradicts the proposition 4.1.2. This eliminates two solutions out of four and gives $\varepsilon_{xy} = 0$ exactly like the linear case. Now the solution of Eq. 115 must be explored, given ε_{xx} and $\varepsilon xy = 0$.

$$\varepsilon_{yy}^2(A + 3B + C) + \varepsilon_{yy}\left[\lambda + 2\mu + \varepsilon_{xx}(2C + 2B)\right] + \lambda\varepsilon_{xx} + \varepsilon_{xx}^2(B + C) = 0. \tag{120}$$

The discriminant,

$$\Delta = \left[\lambda + 2\mu + \varepsilon_{xx}(2C + 2B)\right]^2 - 4(A + 3B + C)\left(\lambda\varepsilon_{xx} + \varepsilon_{xx}^2(B + C)\right) \tag{121}$$

is positive because $\varepsilon_{xx} \ll 1$ and the sign is driven by $\lambda + 2\mu$. This give two solutions,

$$\varepsilon_{yy} = \frac{-\left[\lambda + 2\mu + \varepsilon_{xx}(2C + 2B)\right] \pm \sqrt{\Delta}}{2(A + 3B + C)}. \tag{122}$$

To find the good solution, the Taylor expansion (for A, B, C small enough) will show which one gives the solution for the linear problem,

$$\varepsilon_{yy} = -\frac{\lambda}{\lambda + 2\mu}\,\varepsilon_{xx}. \tag{123}$$

The strain is function of three variables A, B and C. To ease the search for the correct solution, one can take $A = B = C$, and obtain a function of one variable A.

$$\Delta(A) = (\lambda + 2\mu)^2 + 8A(\lambda + 2\mu)\varepsilon_{xx} - 20A\lambda\varepsilon_{xx} + o(A)$$

$$\sqrt{\Delta(A)} = \lambda + 2\mu + 4A\varepsilon_{xx} - A\frac{10\lambda\varepsilon_{xx}}{\lambda + 2\mu} + o(A) \tag{124}$$

With

$$\varepsilon_{yy} = \frac{-\left[\lambda + 2\mu + 4A\varepsilon_{xx}\right] \pm \sqrt{\Delta}}{10A}, \tag{125}$$

it comes that $+\sqrt{\Delta}$ gives the solution. Eventually the unique continuous solution is

$$\varepsilon_{yy} = \frac{-\left[\lambda + 2\mu + \varepsilon_{xx}(2C + 2B)\right] + \sqrt{\Delta}}{2(A + 3B + C)}. \tag{126}$$

From that point it is possible to derive the unknowns $_{0,i}u_x$ and $_{0,i}u_y$ for the non-linear boundary problem,

$$_{0,i}u_x = _{1,i} u_x + \frac{\Delta y}{2\Delta x} \left(_{1,i+1}u_y - _{1,i-1} u_y\right) \tag{127}$$

$$_{0,i}u_y = _{1,i} u_y - \Delta y \frac{-\left[\lambda + 2\mu + \varepsilon_{xx}(2C + 2B)\right] + \sqrt{\Delta}}{2(A + 3B + C)}, \tag{128}$$

with ε_{xx} approximated by $(_{1,i+1}u_x - _{1,i-1} u_x)/(2\Delta x)$.

In order to verify that Prop. 4.1.2 is correct, a P-wave has been simulated. For the continuous solution, the wave travels in the structure. However for other solutions the computation does not simulate a P-wave but a non physical result with very high stress on the ghost cells.

4.1.2.1 Computation at the processor

Even though the exact solution was found above, it is not sufficient for the computation. Indeed the function $\varepsilon_{yy}(A, B, C)$ in Eq. 128 is not defined at $(0,0,0)$, even if the limit exists. Due to computation errors of the processor, this may give some instability to the code particularly if there exist region where non-linear coefficients are small or zero. Because the exact solution is not suitable for computation, another has to be developed from Eq. 128. Using the exact solution and the fact that $\varepsilon_{xx} \ll 1$, a Taylor expansion can form a second order polynomial in ε_{xx}. If the coefficient in front of ε_{xx}^2 has a more suitable expression in terms of A, B and C this will provide an alternative to the exact solution. In that case the Taylor expansion gives,

$$\tilde{\varepsilon}_{yy} \approx - \frac{\lambda}{\lambda + 2\mu} \varepsilon_{xx}$$
$$+ \frac{-2\lambda(A + 3B + C) - 2(\lambda + 2\mu)(B + C) + \lambda(\lambda + 2\mu)(2B + 2C)}{(\lambda + 2\mu)^3} \varepsilon_{xx}^2$$
$$+ o\left(\varepsilon_{xx}^2\right) \tag{129}$$

The Eq. 129 emphasizes a nice expression for A, B and C, because it is defined at every $(A, B, C) \in \mathbb{R}^3$ including 0.

One should note that deriving the Taylor expansion of the exact solution is not very elegant because it implies to know the exact solution. An alternative method is provided here to compute the Taylor expansion of the continuous solution without knowing the exact solution. Indeed it is possible to work directly on the Eq. 115 and 116. Perturbing the linear solution $\tilde{\varepsilon}_{yy} \approx -\frac{\lambda}{\lambda+2\mu} \varepsilon_{xx} + \delta\varepsilon_{yy}$, $\tilde{\varepsilon}_{xy} \approx 0 + \delta\varepsilon_{xy}$ and injected the expressions in the system 115 and 116 yields directly the second order Taylor expansion of the non-linear solution. The method relies strongly on continuity and proposition 4.1.2, because the continuity implies the existence of a Taylor expansion.

In order to choose which one of the two solutions must be implemented in the code, some simulation will help. The strain is evaluation at one point in the structure for P-wave. The common reference for comparison is the linear solution ε_{xx}^0. Firstly the exact solution is computed for A, B, C small compared to the Lamé coefficient. Thus $\lim_{A,B,C\to 0} \varepsilon_{xx}$ means that the non-linear parameter β is small, here $\beta \approx 10^{-10}$.

$$\| \lim_{A,B,C\to 0} \varepsilon_{xx} - \varepsilon_{xx}^0 \| \approx 10^{-9}, \tag{130}$$

while $\|\varepsilon_{xx}\| \approx 10^{-5}$. Secondly the Taylor solution $\tilde{\varepsilon}_{xx}$ is implemented in the code.

$$\|\tilde{\varepsilon}_{xx}(A = B = C = 0) - \varepsilon_{xx}^0 \| \approx 10^{-20}. \tag{131}$$

This computation errors are due to the processor errors.

The Taylor expansion solution is therefore a better solution for computation because it suffers of computational errors.
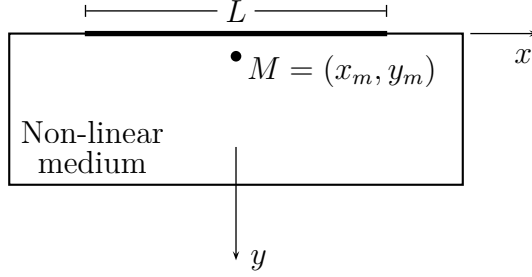
Figure 18: Rectangle geometry of the material for numerical simulations with the excitation on a band $[-L/2; L/2]$ on the top surface.

4.2 Verification of the code

4.2.1 Approximations and criteria

For the non-linear scheme there exist no result on convergence of the algorithm. Thus a comparison between the non-linear code and the analytical solution is required. Fortunately there exists a closed form solution (Eq. 47) for a specific problem. This solution requires several assumptions. Indeed the excitation must be on an infinite surface, the solution is valid in a region close to the surface. This region is described by the Eq. 48,

$$y < \frac{4}{10\beta k} \frac{\lambda + 2\mu}{P} \tag{132}$$

This equation is reformulated here by $y < L^*$, for convenience. The external forcing on an infinite surface can be approached by an excitation on a certain length L of the surface. Point $M = (x_m, y_m)$ records the displacement for each time step. All these considerations are depicted on Fig. 18. Practically, $y_m \ll L/2$, which means that the point M sees an infinite excitation on the surface. Also M is included in the validity region, that is, $y_m < L^*$ because $L < L^*$ will always be verified.

The points $(-L/2, 0)$ and $(L/2, 0)$ radiate spherical waves as depicted on Fig. 19. Thus a time criterion should establish a safe measurement period. Again, because the P-wave has the biggest celerity, the criterion will use it. It comes,

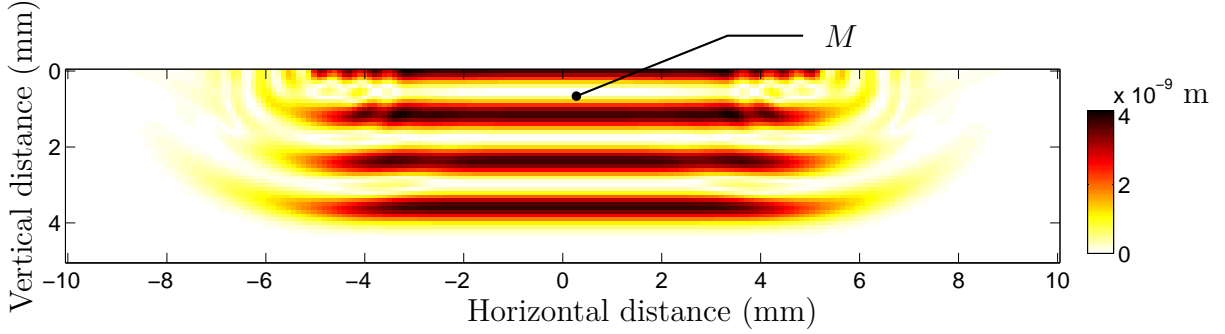$$t < \frac{\sqrt{y_m^2 + (L/2)^2}}{c_P}. \tag{133}$$

47

Figure 19: $u_y(y,t)$ in the whole plate (in meters). Numerical CA simulations approximates plane wave propagation close to the top surface.

Table 6: Excitation proprieties.

Physical quantities	Units	Values
F_0	N	100
f_0	MHz	5

Because the point M is close to the surface $y_m \ll L/2$,

$$t < \frac{L}{2c_P} \lesssim \frac{\sqrt{y_m^2 + (L/2)^2}}{c_P}. \tag{134}$$

4.2.2 Numerical results

The external forcing on the top of the material is a sine wave,

$$F_{\text{excitation}}(t) = F_0 \sin(2\pi f_0 t).$$

Parameters for such an excitation are recalled in table 6.

The physical proprieties of the material are stated in table 7 and the simulation parameters are stated in table 8. These data does not correspond to any particular material. The Lamé coefficients are those of aluminum. However the non-linear constants were chosen arbitrarily but close to typical values.

With a computer equipped with 2GB of RAM and a processor Intel Pentium E2180 at frequency 2.00GHz, the simulation took roughly 30 seconds. The result is presented on Fig. 20. The squared error $SE = 1.1\%$, which shows a good accuracy of the code.

Table 7: Material proprieties.

Physical quantities	Units	Values
ρ	kg.m^{-3}	2700
λ	Pa	$5.04\ 10^{10}$
μ	Pa	$2.59\ 10^{10}$
A	Pa	$1\ 10^{10}$
B	Pa	$1\ 10^{10}$
C	Pa	$1\ 10^{10}$

Table 8: Simulation parameters.

Physical quantities	Units	Values
L_x	cm	2
L_y	cm	1
Δx	m	10^{-4}
Δy	m	10^{-4}
L	cm	1
x_m	m	0
y_m	m	$5\ 10^{-4}$

However this result does not give the accuracy on the non-linear contribution. Indeed the linear term is a lot greater than the non-linear one. Hence this SE represents much more the linear SE.

Fortunately it is possible to investigate the non-linear term (resp. linear terms) $u^{N}L(\vec{x}, t)$ (resp. $u^{L}(\vec{x}, t)$) because it is depending on P^2 (resp. P). Then the solution has the expression,

$$u_+(\vec{x}, t) = u^{L}(\vec{x}, t) + u^{NL}(\vec{x}, t).$$

If the opposite excitation $(P \rightarrow -P)$ is considered, it comes,

$$u_-(\vec{x}, t) = -u^{L}(\vec{x}, t) + u^{NL}(\vec{x}, t).$$

The mean leads to,

$$\frac{u_+(\vec{x}, t) + u_-(\vec{x}, t)}{2} = u^{NL}(\vec{x}, t).$$

Then using these notations (and $\tilde{\ }$ denotes the numerical solution) it comes,

$$SE = \frac{\|u - \tilde{u}\|_2}{\|u\|_2} \approx \frac{\|u^L - \tilde{u}^L\|_2}{\|u^L\|_2} \tag{135}$$
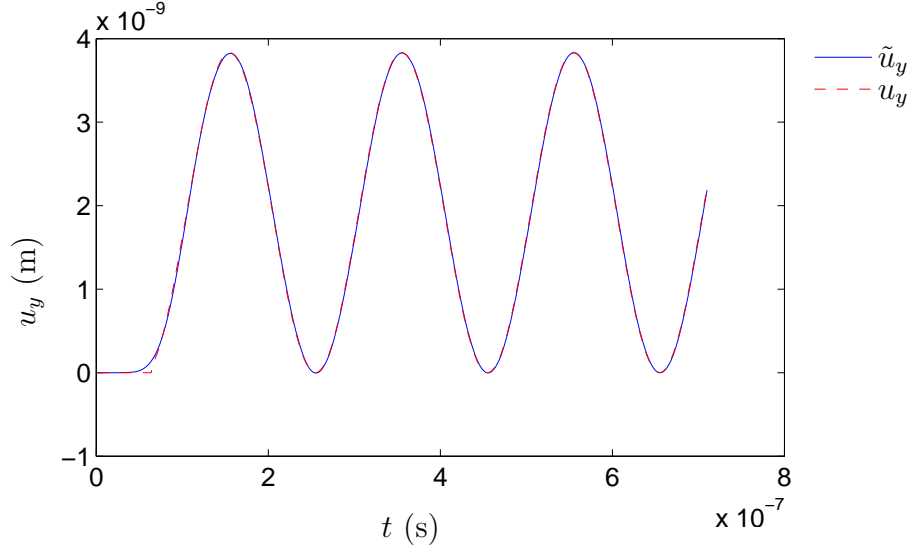
Figure 20: Non-linear simulation for the case described above

The separation of the two terms allows to compute the accuracy on the non-linear contribution. The result is given on Fig. 21. The non-linear squared error, is defined by,

$$SE_{NL}^2 = \frac{\|u^{NL} - \tilde{u}^{NL}\|_2^2}{\|u^{NL}\|_2^2}. \tag{136}$$

The numerical experiment shows $SE_{NL} = 2.2\%$ which is very good, because even though non-linearities are small the CA code keeps accurate computation.

Figure 21: Non-linear terms isolated from the whole expression of the displacement

CHAPTER V

LAMB WAVES

In this chapter the theory of linear guided wave is outlined. This theory uses both the mode formalism and the wave formalism for solving wave equation. The exact trave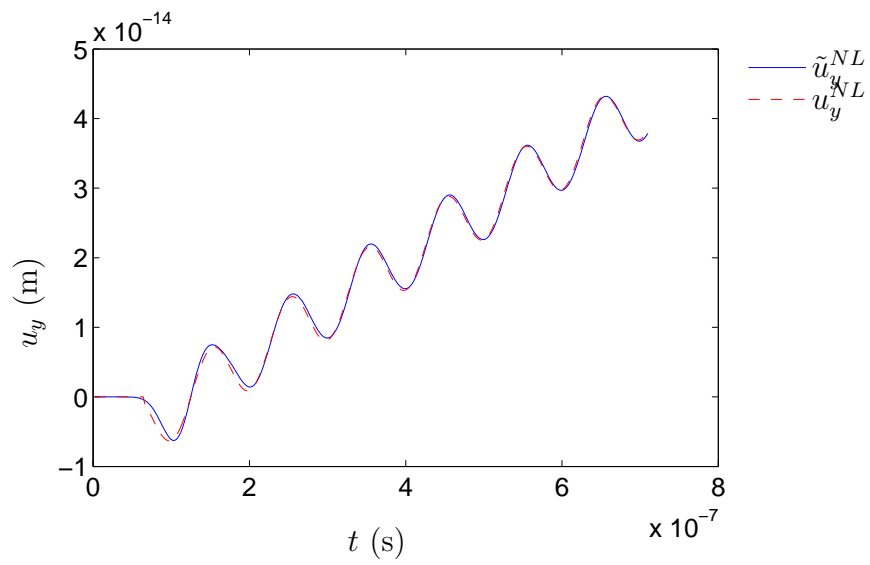ling mode solutions are derived and implemented in the CA code. This will be a new occasion to test the code, particularly for dispersion curves and reflection on a free stress edge.

5.1 Theory

5.1.1 Wave equations

The material with the geometry depicted on Fig. 22 is considered in this chapter. This rectangle has one dimension L_x much bigger than the other one L_y i.e. $L_y \ll L_x$. From that point one may imagine a wave traveling along the $x-$axis.

It is not necessary to consider the $z-$dimension, because the problem has two dimensions. Then, the only variables to consider are x, y and t. The displacement is given by:

$$\underline{u} = \begin{pmatrix} u_x(x,y,t) \\ u_y(x,y,t) \\ 0 \end{pmatrix} \tag{137}$$

Then the strain $\underline{\varepsilon}$ is computed by,

$$\underline{\underline{\varepsilon}} = \begin{pmatrix} \frac{\partial u_x}{\partial x} & 1/2\left(\frac{\partial u_y}{\partial x} + \frac{\partial u_x}{\partial y}\right) \\ 1/2\left(\frac{\partial u_y}{\partial x} + \frac{\partial u_x}{\partial y}\right) & \frac{\partial u_y}{\partial y} \end{pmatrix} \tag{138}$$

After that, the Hooke's law 56 allows to compute the stress $\underline{\sigma}$. And finally the wave equation is derived from the Newton's second law.

$$\underline{\mathrm{div}}\ \underline{\underline{\sigma}} + \underline{f}^{\mathrm{external}} = \rho\underline{\gamma}. \tag{139}$$
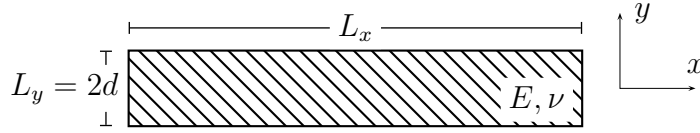
Figure 22: Material geometry

Without considering any external forces the previous equations can be transformed in (see [8]):

$$(\lambda + \mu) \left(\frac{\partial^2 u_x}{\partial x^2} + \frac{\partial^2 u_y}{\partial x \partial y} \right) + \mu \left(\frac{\partial^2 u_x}{\partial x^2} + \frac{\partial^2 u_x}{\partial y^2} \right) = \rho \frac{\partial^2 u_x}{\partial t^2} \tag{140}$$

$$(\lambda + \mu) \left(\frac{\partial^2 u_x}{\partial x \partial y} + \frac{\partial^2 u_y}{\partial x^2} \right) + \mu \left(\frac{\partial^2 u_y}{\partial x^2} + \frac{\partial^2 u_y}{\partial y^2} \right) = \rho \frac{\partial^2 u_y}{\partial t^2} \tag{141}$$

On the right hand side of the equal sign the operators have two derivations with respect to the time t. On the left hand side there are two derivation with respect to the space. This is typical of a wave equation. One of the classical techniques to solve the equations and show the mode is to use the separation of variables. But these two equations are coupled because the terms u_x and u_y appear in both equations.

An alternative approach consists in using scalar potential φ and the potential vector ψ. This method will lead to two uncoupled equations. Physically, there are two phenomena. The material particle is subjected to compression and shear. Then the displacement is a combination of the two, such that each potential is representative of one phenomenon. This distinction will lead to separation of variables in the equation.

We define the displacement by

$$\underline{u} = \underline{\text{grad}} \; \varphi + \underline{\text{curl}} \; \underline{\psi}. \tag{142}$$

The cartesian coordinates allow to use the nabla (∇) operator for grad and curl.

$$\underline{u} = \underline{\nabla} \varphi + \underline{\nabla} \times \underline{\psi}. \tag{143}$$

53

Because $\partial/\partial z = 0$ it becomes,

$$u_x = \frac{\partial \varphi}{\partial x} + \frac{\partial \psi_z}{\partial y} \tag{144}$$

$$u_y = \frac{\partial \varphi}{\partial y} - \frac{\partial \psi_z}{\partial x}. \tag{145}$$

ψ_z is noted ψ for convenience. Using equations 141 yields,

$$(\lambda + 2\mu)\nabla^2 \varphi = \rho\, \ddot{\varphi} \tag{146}$$

$$\mu \nabla^2 \psi = \rho\, \ddot{\psi} \tag{147}$$

The 2D Laplacian $\nabla^2(\cdot)$ operator could be written as $\nabla^2(\cdot) = \partial^2(\cdot)/\partial x^2 + \partial^2(\cdot)/\partial y^2$. The equation corresponds to the P-wave, while the second equation corresponds to S-waves, where S stands for shear. This wave is known as a transverse wave,

$$c_P^2 = \frac{\lambda + 2\mu}{\rho} \tag{148}$$

$$c_T^2 = \frac{\mu}{\rho}. \tag{149}$$

These equations yield,

$$\frac{\partial^2 \varphi}{\partial x^2} + \frac{\partial^2 \varphi}{\partial y^2} = \frac{1}{c_P^2} \frac{\partial^2 \varphi}{\partial t^2} \tag{150}$$

$$\frac{\partial^2 \psi}{\partial x^2} + \frac{\partial^2 \psi}{\partial y^2} = \frac{1}{c_T^2} \frac{\partial^2 \psi}{\partial t^2} \tag{151}$$

It is clear that the method has produced two uncoupled equations. This set of equations is completed with boundary conditions on the stress or displacement. The free stress boundary conditions on top ($y = d$) and bottom ($y = -d$) surface leads to $\sigma_{yy}(y = \pm d, x, t) = \sigma_{xy}(y = \pm d, x, t) = 0$. For the left and right hand side, the boundary conditions will be discussed later.

5.1.2 Lamb waves

The usual method to solve the wave equations is to suppose separation of variables. Thus the solution will be presented as the product of three independent functions for

the three variables x, y and t. These functions are different, depending on a modal or propagative solution. If the characteristic length of the waves in the material is chosen as the smallest wave length between the P and S wave then L_y has quite the same magnitude as the characteristic length, but L_x is much greater. Thus it is suitable to consider propagative solution only following the $x-$axis and a modal solution on the $y-$axis. These considerations lead to write separation of variables including wave propagation,

$$\varphi(x, y, t) = \Phi(y)e^{i(kx-\omega t)} \tag{152}$$

$$\psi(x, y, t) = \Psi(y)e^{i(kx-\omega t)}. \tag{153}$$

From that point, the goal is to find the mode shape, i.e. $\Phi(y)$ and $\Phi(y)$ and the dispersion relation characteristic of the propagative solution.

By injecting the functions Φ and Ψ in the equations 150 and 151 it comes two second order linear ordinary differential equations. The general solution, in $\mathbb{C}$, are

$$\Phi(y) = A_1 \sin(py) + A_2 \cos(py) \tag{154}$$

$$\Psi(y) = B_1 \sin(qy) + B_2 \cos(qy) \tag{155}$$

where,

$$p^2 = \frac{\omega^2}{c_L^2} - k^2 \quad \text{and} \quad q^2 = \frac{\omega^2}{c_T^2} - k^2. \tag{156}$$

p and q can be complex. For instance the P-wave has the greatest celerity, then the phase velocity $\omega/k < c_P$ gives p complex. The coefficients A_1, A_2, B_1 and B_2 are also consider to be complex.

Without further mathematical derivation, the solution for the propagating modes is quoted from [7]. The expressions 152 and 153 have been injected in the equations

144 and 145. For symmetric modes, displacement and stress are,

$$u_x = ikA_2 \cos(py) + qB_1 \cos(qy), \tag{157}$$

$$u_y = -pA_2 \sin(py) - ikB_1 \sin(qy), \tag{158}$$

$$\sigma_{xy} = \mu \left(-2ikpA_2 \sin(py) + (k^2 - q^2)B_1 \sin(qy) \right), \tag{159}$$

$$\sigma_{yy} = -\lambda(k^2 + p^2)A_2 \cos(py) - 2\mu \left(p^2 A_2 \cos(py) + ikqB_1 \cos(qy) \right). \tag{160}$$

For antisymmetric modes, displacement and stress are,

$$u_x = ikA_1 \sin(py) - qB_2 \sin(qy), \tag{161}$$

$$u_y = pA_1 \cos(py) - ikB_2 \cos(qy), \tag{162}$$

$$\sigma_{xy} = \mu \left(2ikpA_1 \cos(py) + (k^2 - q^2)B_2 \cos(qy) \right), \tag{163}$$

$$\sigma_{yy} = -\lambda(k^2 + p^2)A_1 \sin(py) - 2\mu \left(p^2 A_1 \sin(py) - ikqB_2 \cos(qy) \right). \tag{164}$$

The complex allow to derive the very general form of the solution. The real solution may contain cosh instead of cos or sinh instead of sin.

5.1.3 Dispersion curves

The dispersion relation comes out by applying the boundary conditions for the two stress systems above. The free stress boundary conditions are $\sigma_{yy}(y = \pm d, x, t) = \sigma_{xy}(y = \pm d, x, t) = 0$. The system of equations 159 and 160 and the boundary conditions give a system of two equations with two unknowns A_2 and B_1 equal to zero. For nontrivial solution the determinant of that system must be zero. The equation gives the dispersion relationship for symmetric modes. Thus A_2 depends on B_1 (or the contrary) with a single equation. Same holds for the antisymmetric modes.

For symmetric modes the dispersion relation is

$$\frac{\tan(qd)}{\tan(pd)} + \frac{4k^2 pq}{(q^2 - k^2)^2} = 0, \tag{165}$$

and for antisymmetric modes

$$\frac{\tan(qd)}{\tan(pd)} + \frac{(q^2 - k^2)^2}{4k^2 pq} = 0. \tag{166}$$
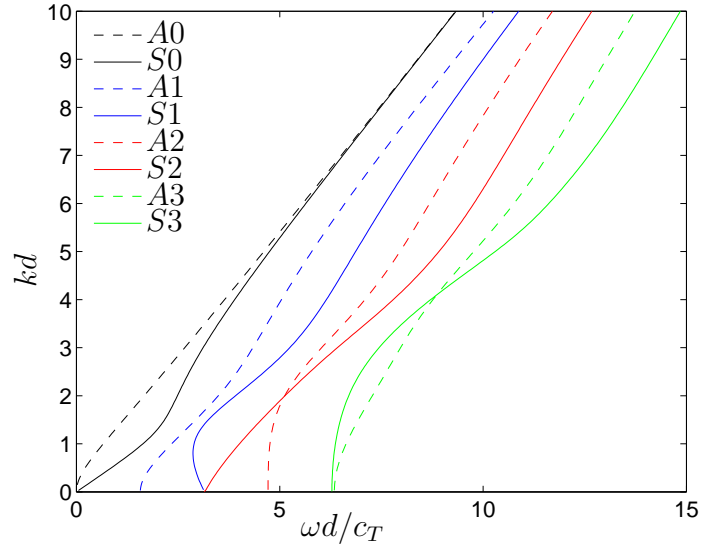
Figure 23: Dispersion curves of the Lamb waves for the material described in table 9.

The dispersion curves are computed from the two dispersion relations. It is possible to show that the dispersion relations only depends on the Poisson's ratio . This point is explained in detail in the subsection 5.2.1.

An example is treated in the table 9. The dispersion curves for the material described in table 9 are depicted on Fig. 23. The software DISPERSE provided these

Table 9: Material properties for dispersion curve computation.

Physical quantities	Units	Values
ρ	kg.m^{-3}	2700
λ	Pa	5.4941 10^{10}
μ	Pa	2.6452 10^{10}
c_P	m.s^{-1}	6320
c_T	m.s^{-1}	3130
d	m	0.8 10^{-3}

curves. The ω (resp. k) has been replaced by $\omega d/c_T$ (resp. kd) because it is easier to manipulate quantities with no dimension.

57

5.2 Numerical simulations

Now that the theory has been explored it is necessary to work on practical aspects of the problem. For the simulation of Lamb wave propagation in a plate, several points have to be treated. Firstly, the mode shape must be derived in the real domain $\mathbb{R}$. Secondly the numerical resolution must be computed for simulation. Finally, the external forcing has to be implemented in the code and tested.

5.2.1 Selection of one mode

This paragraph explores a method for determining all the parameters $(p, q, k$ and $\omega)$ for a chosen mode. First the frequency is given. For simplicity $S0$ mode is studied because it can exist under all the frequency of other modes. For

$$\frac{\omega d}{c_T} = 1, \tag{167}$$

the parameters p and q are,

$$q^2 = \frac{1}{d^2} - k^2 \tag{168}$$

$$p^2 = \frac{\gamma^2}{d^2} - k^2, \quad \text{wherein } \gamma = \frac{c_T}{c_P}. \tag{169}$$

For this given frequency ω there exist two possibilities for the wavenumber k, one for the mode $A0$ and one for the mode $S0$. The reader can draw a vertical line on the Fig. 23 for the frequency $\omega d/c_T$ and see that it intersects two dispersion curves. After selecting the $S0$ mode the equation 165 must be solved for the unknown k.

Before continuing, the variables in the equation 165 must be change to get rid of the physical dimension. Let the unknown X replace the wave number, $X = (kd)^2$. The equation 165 becomes

$$\frac{\tan \sqrt{1 - X}}{\tan \sqrt{\gamma^2 - X}} + \frac{\sqrt{\frac{1}{X} - 1} \sqrt{\frac{\gamma^2}{X} - 1}}{\left(\frac{1}{4X} - 1\right)^2} = 0. \tag{170}$$

The MATLAB solver gives $\sqrt{X} = kd = 0.5852$. Then computation of the different parameters are given in table 10.

Table 10: $S0$ mode parameters.

Physical quantities	Units	Values
ω	s^{-1}	$3.9125 \ 10^6$
k	m^{-1}	731
p	m^{-1}	$390i$
q	m^{-1}	1014

Remark 5.2.1. The equation 170 emphasizes the parameter γ. From the definition of the celerities and the Lamé coefficients it comes,

$$\gamma = \sqrt{1 - 2\nu} \tag{171}$$

Thus the dispersion curves only depends on the Poisson's ratio, ν.

After selecting one mode, it is possible to determine a relation between the different coefficients. For the $S0$ symmetric mode there is the set of equations 159 and 160. Applying the free stress boundary conditions gives,

$$\begin{pmatrix} \sigma_{xy} \\ \sigma_{yy} \end{pmatrix} = M(y = \pm d) \begin{pmatrix} A_2 \\ B_1 \end{pmatrix} = 0. \tag{172}$$

The matrix $M(y)$ is a square matrix of four elements $M_{ij}(y)$. All of them are functions of the variable y. Because the trivial solution is not interesting, $\det M(y = \pm d) = 0$. One should easily remark that this determinant is an even function of the variable d, which gives only one equation: the dispersion equation. The same is true for the antisymmetric modes. Because the system is neither invertible nor trivial ($M(y = \pm d) = 0$) the coefficients A_2 and B_1 are proportional. In other words the rank of the matrix is 1. The link between A_2 and B_1 is established by writing the first line of the system,

$$M_{11}(+d) \ A_2 + M_{12}(+d) \ B_1 = 0, \tag{173}$$

then,

$$B_1 = -\frac{M_{11}(+d)}{M_{12}(+d)} A_2. \tag{174}$$

59

More explicitly there is,

$$B_1 = \frac{2ikp\sin(pd)}{(k^2 - q^2)\sin(qd)} A_2, \tag{175}$$

then, because p has zero real part as shown in table 10, it yields

$$B_1 = -\frac{2ik\mathrm{Im}(p)\sinh(\mathrm{Im}(p)d)}{(k^2 - q^2)\sin(qd)} A_2. \tag{176}$$

This equation should finish to explicit the link. However there still exists one point that must be clarified. The coefficients A_2 and B_1 are complex. The equation 176 can be separated into a set of two equations,

$$\mathrm{Re}(B_1) = \frac{2k\mathrm{Im}(p)\sinh(\mathrm{Im}(p)d)}{(k^2 - q^2)\sin(qd)}\mathrm{Im}(A_2) \tag{177}$$

and

$$\mathrm{Im}(B_1) = -\frac{2k\mathrm{Im}(p)\sinh(\mathrm{Im}(p)d)}{(k^2 - q^2)\sin(qd)}\mathrm{Re}(A_2). \tag{178}$$

The system 159 and 160 shows that some constants are complex while others are real. Thus, the expression can be real by using whether $\mathrm{Re}(A_2)$ (resp. $\mathrm{Re}(B_1)$) or $\mathrm{Im}(A_2)$ (resp. $\mathrm{Im}(B_1)$).

Now that the link between B_1 and A_2 is established, one of the two can be chosen arbitrarily. For instance during simulation $\mathrm{Re}(A_2)$ and $\mathrm{Im}(A_2)$ are set to the same value (but can be different) which gives immediately the shape of the mode. For the $S0$ mode with $\mathrm{Re}(A_2) = \mathrm{Im}(A_2) = 10^{-10}$ the mode has the shape depicted on figure 24.

5.2.2 Numerical resolution for the $S0$ mode

This paragraph supposed that the material is the same as describe before. The dispersion curves are given by the Fig. 23.

The time resolution Δt is determined by the formula from a previous chapter,

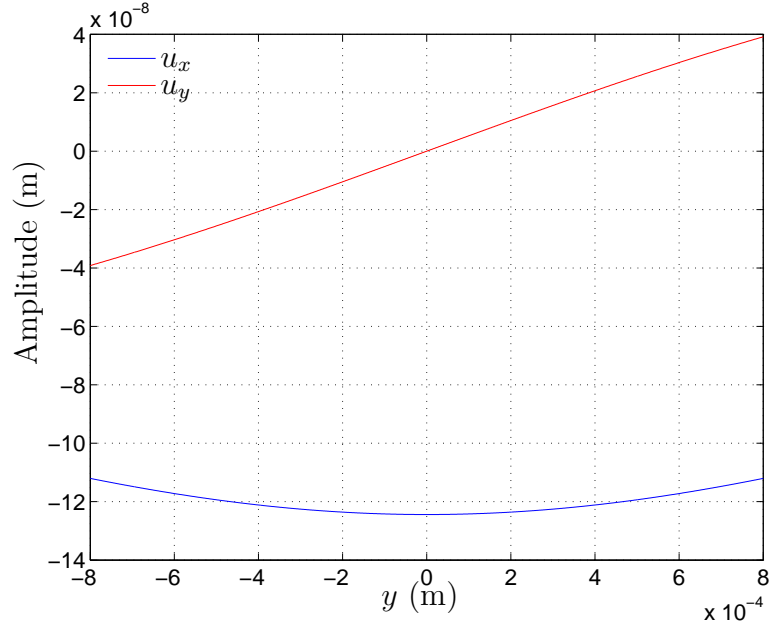$$\Delta t = \min\left(\frac{1}{f_{\mathrm{sampling}}}, \frac{\Delta y}{10\ c_P}\right).$$

Figure 24: $S0$ mode shape (u_x, u_y) at frequency $\omega = c_T/d$. The displacement u_x is symmetric whereas the displacement u_y is antisymmetric which is confirmed by the equations 157 and 158.

Concerning the space resolution Δx,

$$\Delta x = \frac{2\pi}{10\ k},\tag{179}$$

where $2\pi/k$ is the wavelength of the Lamb wave propagation along the $x-$axis. For the spatial resolution Δy the approach is different. This term will be small enough so it is possible the "see" the lamb modes. It strongly depends on the shape of the mode. For example if the mode is a sine, the sampling frequency will be ten times higher than the spatial frequency. If the mode is a sinh or cosh the resolution can be chosen ten times smaller than the minimum of the radius of curvature. Practically one can draw the exact solution and then sampled solution and compared the two. This gives a very fast way to establish Δy. The numerical resolution is presented in table 11

Table 11: Numerical resolution for computation of the $S0$ mode at the frequency $\omega = c_T/d$.

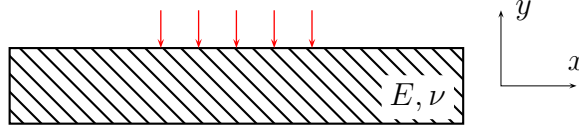| Physical quantities	Units	Values
Δt	s	$5.21 \ 10^{-9}$
Δx	m	$9.41 \ 10^{-5}$
Δy	m	$3.3 \ 10^{-4}$

Figure 25: Comb external forcing on the top of the plate. The stress is located at several points separated the wavelength of the corresponding Lamb mode.

5.2.3 Source waveform

This paragraph discusses the external forcing that will send lamb waves in the material. The expression of the forcing will contain a sine at the good frequency ω. However the numerical simulation forces to have a signal finite in time or at least L_2−integrable on $\mathbb{R}$. The sine is then multiplied by a Gaussian to match that condition. The spectrum will be widened. Thus

$$F_{\text{external}}(x, y, t) = \frac{1}{\sqrt{2\pi\sigma^2}}\exp\left(-\frac{(t - t_0)^2}{2\sigma^2}\right) \ e^{-i\omega t} \ \Upsilon(x, y),\qquad(180)$$

where Υ is a function depending only on geometric variables x and y. It can be vectorial if necessary. The difficult point is to choose the function Υ because this function must select one of the modes $S0$ or $A0$ and inject the correct one in the structure.

The first solution is to excite the mode at several points on the surface, as shown on Fig. 25. The points are distant by the wavelength. This method used in experiment is called the "comb". Then Υ is defined by

$$\Upsilon(x) = \begin{cases} 1 \text{ if } x = 0, \ \lambda, \ 2\lambda \ \ldots \ n\lambda \\ \\ 0 \text{ elsewhere} \end{cases}.\qquad(181)$$
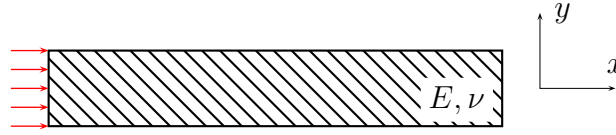
Figure 26: Modal forcing on the left free edge. The whole surface is submitted to the exact Lamb mode stress.

The Υ can also be seen as the characteristic function of the set 0, λ, $\ldots$ $n\lambda$, sometimes called the comb function . This method is based on resonance excitation, [19]. Even though there is no theoretical solution for such an external forcing, but it is intuitive to know that if several modes are excited the biggest in amplitude will correspond to $S0$. One must recognize that this procedure is not very precise but it is very useful for experiment because it is an external forcing on the boundary. Another way to send the mode in the structure is describe below.

In order to excite a single mode at the given frequency, another approach must be developed. The function Υ is chosen as the mode shape. This procedure has already been explored in [15]. It consists in implementing the mode shape as displacement constraint on one of the two free edges of the plate. These boundary external forcing should replace a wave coming from the infinite in the sense that if such a wave arrive on the cells this would make no difference with the finite problem considered here. On Fig. 26, a finite plate is excited on the left edge. On that figure several red arrows represent that forcing occurring at several point. This discretization is directly related to the material cell discretization, because every cell on the left edge are submitted to such a boundary condition. Thus it is, now, possible to write the new forcing term Υ at $x = 0$,

$$
\mathrm{Re}\,\Upsilon(0,y)\mathrm{e}^{-i\omega t} = \mathrm{Re}\left(\begin{array}{c} \mu\left(-2ikpA_2\sin(py) + (k^2 - q^2)B_1\sin(qy)\right) \\ -\lambda(k^2 + p^2)A_2\cos(py) - 2\mu\left(p^2 A_2\cos(py) + ikqB_1\cos(qy)\right) \end{array}\times\mathrm{e}^{-i\omega t}\right)
\tag{182}
$$

As the mode $S0$ was studied before, the Υ is then derived in the real domain $\mathbb{R}$.

63

For this case the p parameter is pure complex while the q parameter is real. From equation 176, $A_2 \in \mathbb{R}$ is chosen arbitrarily which yields $B_1 \in \mathbb{C}$ with zero real part. It comes,

$$p = i \, \text{Im}(p), \tag{183}$$

$$q \in \mathbb{R}, \tag{184}$$

$$A_2 \in \mathbb{R}, \tag{185}$$

$$B_1 = i \, \text{Im}(B_1). \tag{186}$$

Then using equation 182 the real solution is, for the x component,

$$\text{Re}\left(\Upsilon(0,y)\text{e}^{-i\omega t}\right)_x = \mu\left[2k\text{Im}(p)A_2\sinh(\text{Im}(p)y) + (k^2 - q^2)\text{Im}(B_1)\sin(qy)\right]\sin(\omega t), \tag{187}$$

and for the y component,

$$\text{Re}\left(\Upsilon(0,y)\text{e}^{-i\omega t}\right)_y =$$
$$- \lambda(k^2 - \text{Im}(p)^2)A_2\cosh(\text{Im}(p)y)\cos(\omega t)$$
$$- 2\mu\left(-\text{Im}(p)^2 A_2\cosh(\text{Im}(p)y) - kq\text{Im}(B_1)\cos(qy)\right)\cos(\omega t). \tag{188}$$

These two equations are discretized on the vertical grid Δy and computed at every step of time Δt, to be implemented in the CA code,

$$\text{Re}\left(\Upsilon(0, j\Delta y)\text{e}^{-i\omega n\Delta t}\right)_x \quad \forall j \in [\![0, N_y]\!], \ \forall n \in [\![0, \infty[\![\tag{189}$$

$$\text{Re}\left(\Upsilon(0, j\Delta y)\text{e}^{-i\omega n\Delta t}\right)_y \quad \forall j \in [\![0, N_y]\!], \ \forall n \in [\![0, \infty[\![\tag{190}$$

The last two equations are those directly implemented in the code.

5.2.4 Simulations

Simulations have demonstrated that a wave packet travels inside the plate. Fig. 27 emphasizes this traveling wave packet of $A1$ modes. With the color rate it possible to see that the wave at the beginning and the end are weak compared to the center. The
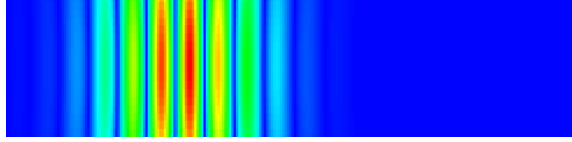
Figure 27: Simulation of the Lamb mode $A1$ propagating in the structure. The color gradient underlines the von Mises stress in the material. The external forcing is located on the left free edge.

effect of the Gaussian modulation give the explanation. The duration of simulation for such a wave strongly depends on the mode frequency, because the time step is related to the sampling frequency which also depends on the frequency of the wave. For instance doubling the mode frequency will divide the time step by 2.

5.2.4.1   Signal processing and dispersion analysis

In order to analyze Lamb mode in the structure, the Fourier transform is an efficient tool for identifying terms. In [2], Alleyne and Cawley present a method based on Fourier transform and finite elements to separate modes. Indeed when a periodic signal is a superposition of different periodic subsignals at different frequencies, Fourier transform allows a clear separation of each contribution. Moreover a wave that propagates can be written has a sum of exponentials $e^{i(kx-wt)}$. Because of the product of two exponentials it necessary to use the two-dimensional Fourier transform. In [15] the authors apply this technique to Lamb waves in order to isolate reflected modes.

The CA code allows to compute and save displacement anywhere in the material. For our problem the simulations will save the normal displacement $u_y(x, y = +d, t)$ on the top edge, $\forall x \in [0, L_x]$, at every instant of time, $\forall t$. The result is stored in a matrix U_y. Each line of this matrix corresponds to an instant of time while each column corresponds to a physical point on the top free surface. Taking the 2D FFT will compute the approximated Fourier transform $\tilde{\tilde{U}}_y(\omega, k)$ of the signal U_y. On Fig. 28 the 2D FFT of mode A1 is shown before it reach the boundary. The mode $A1$ is studied here because it may exist with other modes at the frequency $\omega d/c_T = 3$.
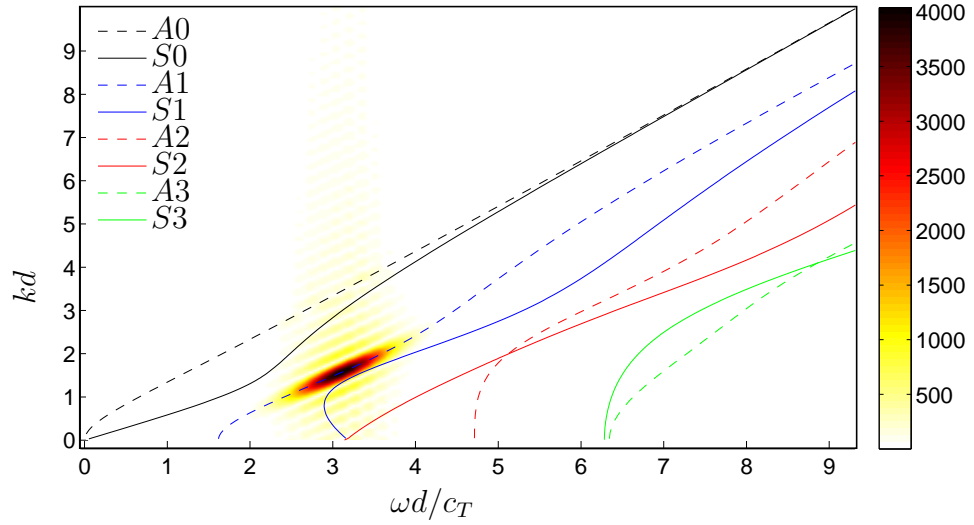
Figure 28: 2D FFT of the signal on the top surface. To the result is superimposed the dispersion curves. The color bar shows the amplitude of the signal. The mode $A1$ travels in the structure.
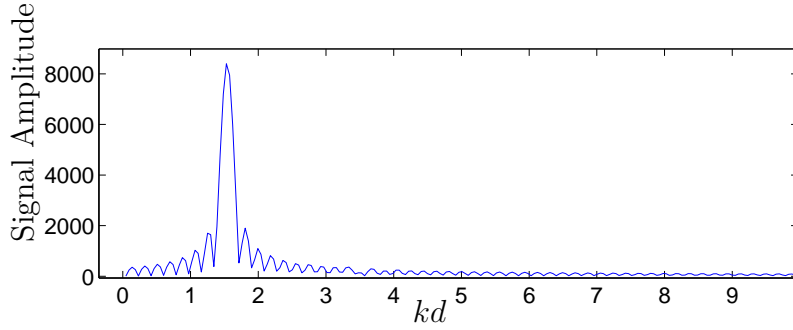

Figure 29: 1D FFT of the signal at the fixed frequency $\omega = 3c_T/d$. The spectrum shows the presence of the $A1$ mode in structure without other modes.

The matrix $\widetilde{\widetilde{U}}_y$ shows a single oval shape centered on frequency and wavenumber of the corresponding mode. This may be explained by the finite extant of the time signal, sine modulated by a Gaussian. Also the FFT tends to widen the real spectrum of the signal. To verify that there is no other mode at this frequency it is convienent to extract the vertical line of the matrix $\widetilde{\widetilde{U}}_y(\omega, k)$ for $\omega d/c_T = 3$. Fig. 29 emphasizes the only existing mode $A1$. The side lobes around the central frequency are due to the FFT algorithm that computes an approximation of the Fourier Transform.

5.2.4.2 Matching with the dispersion curves

Even though, Fig. 28 shows promising result it can not be used to verify the dispersion curves. In the previous paragraph several reasons are stated in order to explain the wide spectrum. There exist several possibilities to sharpen the spectrum given by the FFT. Firstly, the signal length can be increased by using a wide Gaussian curve. The FFT will work on a signal that has more periodic content and therefore will highlight more the single frequencies. The drawback of the method is the long time of simulation. Moreover the material size may also be widen. For propagating wave, the size be must increased also to avoid multiple reflections. It can also be mentioned that a bigger signal requires more time to apply different algorithms such as preprocessing or FFT. Secondly, it would be more efficient to concentrate on the signal itself. Indeed for a single or several separated peaks the FFT will present a global maximum. The argument of the maximum, i.e. the couple (ω, k), is the interesting data. Hence the coordinates of the maximum should be located on (or close to) the dispersion curves. The interesting data is then,

$$\arg\max_{\omega, k} \tilde{\tilde{u}}_y(\omega, k), \tag{191}$$

approximated by,

$$\arg\max_{\omega, k} \tilde{\tilde{U}}_y(\omega, k). \tag{192}$$

This method allows to proceed reasonable simulations in terms of time and keeps accuracy.

The signal obtained after simulations is the matrix U_y. It contains a traveling wave without any reflections at single frequency. This condition guaranties the existence of only one peak in the spectrum. The longest simulations may take 10 minutes and output file might reach the size of 50 MB. Then working with the second method yields a MATLAB algorithm that consists in computing the 2D-FFT, and using the function `max`. This two consecutive functions yields the result in an efficient time,
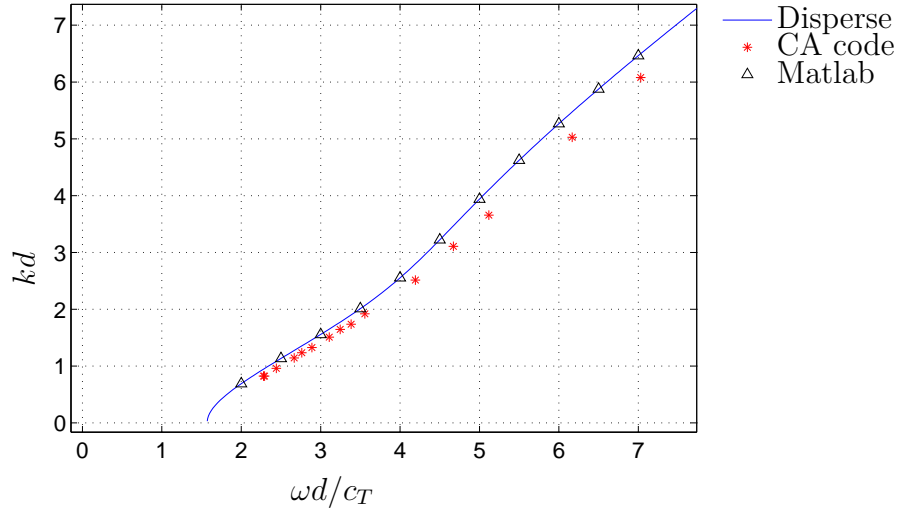
Figure 30: Comparison of the dispersion curve of the $A1$ mode, obtained from the software DISPERSE, the CA code and MATLAB solver.

less than 10 seconds.

This numerical experiment is repeated for different frequencies. For each computation the parameters p and q are calculated considering the $A1$ mode. The results presented on figure 30 are compared to the software DISPERSE and MATLAB solver.

The results shows a good correspondence between the three curves. The MATLAB solver perfectly matches the dispersion curves obtain by disperse. The CA code seems to be less accurate as the frequency the reach $\omega d/c_T = 4$. A higher spatial and time resolution would probably solve that. One should remark that these two softwares directly solve the dispersion equation whereas the CA code simulate a wave physics propagation.

5.2.5 Improvement of the results

Even though the numerical results seem good, a technique is explored here to improve the comparison on Fig. 30. The convergence theorem indicates that a smaller grid and a smaller time step will improve the correspondence between theoretical and computational curves (CA). Thus, taking advantage of that theorem, a numerical experiment was performed on the mode $A1$. This consists in the exact same experiment as the one
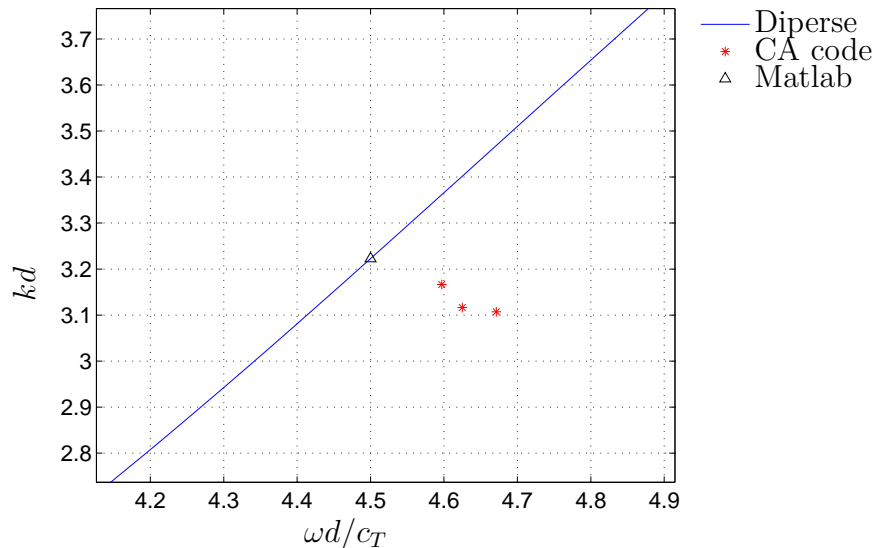
Figure 31: Comparison of the dispersion curve of the $A1$ mode, obtained from the software DISPERSE, the CA code and MATLAB solver. CA is improved by choosing a smaller grid and a smaller time step

in the previous paragraph expect that only one frequency is considered, $\omega d/c_T = 4.5$. The starting point is on the right with the parameter $(\Delta x, \Delta y, \Delta t)$, then the second point has $(\Delta x/2, \Delta y/2, \Delta t/2)$ and the third point has $(\Delta x/4, \Delta y/4, \Delta t/4)$. Each simulation gives a point closer to the other curves considered as theoretical curves.

This experiment demonstrates that simulation can be improved, which is a consequence of the convergence theorem.

5.3 Reflection of the A1 single mode

This section will provide an overview of the amplitude reflection for unique lamb mode $A1$ using the CA code. The signal processing after computation is the same as in the previous section.

5.3.1 Theory and procedure

An A (resp. S) mode will be converted in an A (resp. S) mode. Consequently if one desire to observe reflection of a lamb mode he needs to work at frequency high
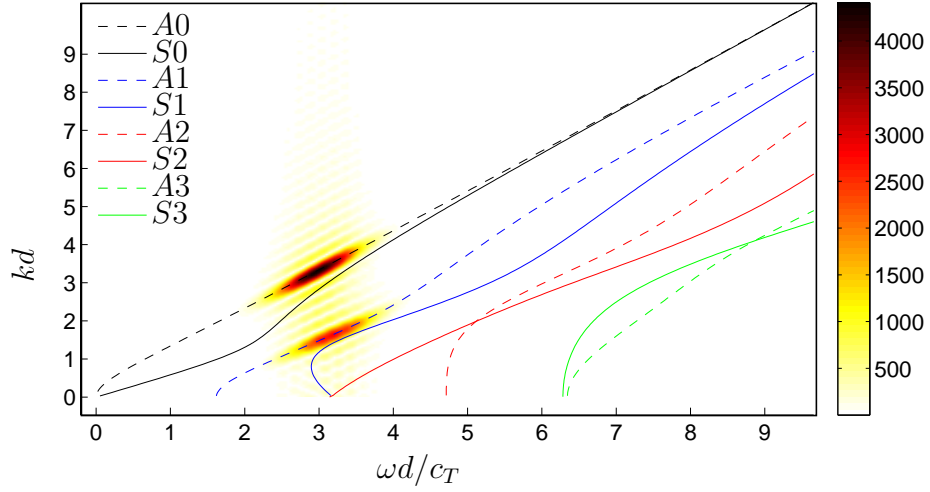
Figure 32: 2D FFT of the signal on the top surface. To the result is superimposed the dispersion curves. The color bar shows the amplitude of the signal. The modes $A0$ and $A1$ travel in the structure after reflection.

enough in order to have two modes of the same type, A or S. To start the simulation and to avoid multiple reflected modes the frequencies considered here are between $\omega d/c_T = 2$ and $\omega d/c_T = 3.5$. At that specific frequency, the mode $A2$ may exist but not as the result of a reflection, the article [15] shows that the reflection coefficient in energy is zero. This guarantees that only $A0$ and $A1$ will be present after reflection, as depicted on Fig. 32. Thus a single mode conversion will be observed here.

The material is divided into two parts. One part is all the material in the box $[0, 2/3\ L_x[$ and the second part is the rest of the material, that is $]2/3\ L_x, L_x]$. The second domain is the acquisition domain, in which the data is collected. For each simulation, that incident wave packet arrives inside the acquisition domain then is reflected on the edge $x = L_x$ and finally goes out of that domain. This procedure allows to have the same distance traveled by the incident and reflected wave. Then the FFT resolution should be the same for incident and reflected wave, ensuring same precision.
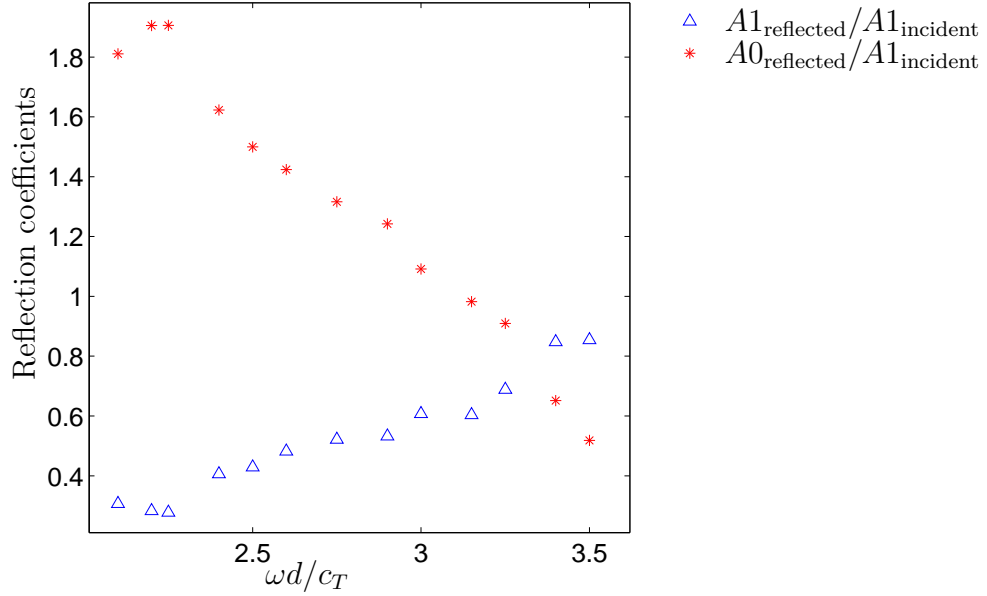
Figure 33: Reflection coefficient for an incident $A1$ mode. The possible reflected wave are $A1$ and $A0$.

5.3.2 Results

The results are presented on Fig. 33. At the frequency $\omega d/c_T = 2$ most of the $A1$ wave is reflected into the $A0$. As the frequency increases the $A1$ reflected mode gets bigger while the $A0$ gets smaller. The two reflections coefficients are equal at the frequency $\omega d/c_T = 3.3$, as the two curves intersect. This intersection is predicted by [15], when the authors look at energy reflection coefficients.

The existence of a reflected $A2$ mode is not observed as expected.

5.3.3 Conclusion

The CA code has shown its capability to simulate lamb waves. An excitation method has allowed to selected a specific mode inside the structure. Once this preliminary work done, the dispersion curves is verified for such a mode. The reflection of Lamb waves was also explored and underlines the accuracy of the code.

CHAPTER VI

CONCLUSION

This research is interested in simulation of wave propagation in a non-linear material material using a novel tool called Cellular Automata.

Theoretical solutions for such a problem were found in particular cases, guided waves [6] and the P-wave [16]. However when the geometry is complicated there is a lack of theoretical predictions. Thus it is necessary to turn towards computational simulation. Leamy developed an original approach [12] for wave propagation in solid linear material, Cellular Automata. This research sought to change the exciting code for non-linear material found in the industry such as aluminum. The first step was to show the stability of the CA code. Thanks to a posteriori correspondence between CA and finite difference (FD) it is possible to use the theoretical tools of FD method. This proof of stability involves work on the eigenvalues of the discrete system of equations. The second step is to establish the resolution for the grid that meshes the material. This considerations should be directly related to the wavelength of the propagating wave. The time step will be chosen, at last, as a compromise between time resolution and stability. The third step is to verify the accuracy of the code. Then the closed form solution of the linear P-wave was compared with the computation of the CA code. Comparisons in terms of displacement and stress show a good accuracy. Results underline a better accuracy for the displacement because CA is strongly based on it and the stress is an intermediate of computation. Thus the displacement will preferred as the data for analysis. The stress will only require to use a thinner grid and a smaller time step, will give also a longer duration for simulations.

Once the linear code is verified it is necessary to add the non-linear material

behavior. Then the theory of non-linear elasticity was explored for problems with two dimensions. It consists in a generalization of the Hooke's law by adding quadratic terms modulated by the Landau and Lifschitz coefficients [11]. This work has provided the non-linear behavior directly implemented in the code. The boundaries require also to be reviewed. In order to have the free stress boundary condition, a non-linear system has to be solve. Using continuity with respect to the non-linear coefficients, a unique solution is chosen out of four possible candidates. Once every practical aspects are solved, the accuracy of this new code must be verified using the same procedure as before. Because the non-linear contribution is much smaller than the linear one, the error function is driven by the linear term. Using pulse inversion technique the non-linear signal is isolated. It consists in exciting the boundary with some stress and then the opposite stress. It yields accuracy even for the non-linear contribution.

Non destructive evaluation prefers to consider Lamb or Rayleigh waves because they may travel over long distance, which is suitable for damage inspection. In the same move, the last part of this thesis inspects the capabilities of the code to simulate Lamb waves. For applications it is necessary to have only one mode, at given frequency, traveling in the thin plate. This mode is excited by a displacement boundary condition. This condition is the exact displacement of the corresponding mode. For verification, the normal displacement to the surface is measured for each time step. With such data, the 2D FFT allows to compute the dispersion curves. This processing was originally established by Cawley [2] for finite elements simulation. However this procedure procedure must be completed by more signal processing because the previous is not accurate enough. Instead of giving a Dirac the FFT gives side lobes and a main peak. Thus the arguments of such a peak are extracted from the data in order to give its localization close to the dispersion curves. After several numerical experiments, the code shows its capability to obtain the dispersion curves. It is also important to know the results are improved with a thinner grid which is expected

by previous simulations. In the continuity of this work, the code may predicts mode conversion as the wave reach a stress free boundary for instance. On that occasion the $A1$ mode was send against that boundary. Identification of mode was operated with the 2D FFT. Values of different incident and reflected peaks were computed as well as the reflection coefficients, for several frequencies.

The Cellular Automata has shown its strong potential to predict was propagation in different configurations. Also the non-linear behavior keeps good accuracy of the code. These features should be combined in order to simulate Rayleigh waves and Lamb waves in a non-linear material. The flexibility of CA code suggest to investigate complicated geometries with scatterers as industry pieces.

APPENDIX A

PROCESSING ON RAW COMPUTATIONAL DATA

In this appendix, a code is presented. After computation of the CA code the data is written in a way such that it is not suitable for direct Matlab processing. The first transformation of the raw data uses Gnu/Linux tools. Indeed these programs are optimized for the operating system and are simple to concatenate.

The raw file is supposed to contains a line with the time and a line with the displacement for instance. The script bellow was written in scriptshell and allows to extract the time from this file.

```
#!/bin/bash
# date:07/27/09
# author:Thibaut Autrusson
# report bugs to thibaut.autrusson@gatech.edu


#catch the number of lines in the file
nblines=$(wc -l data/uY.dat | gawk -F"␣" '{print $1}' )
nbiter=$(( $nblines /494))
nbiter2=$(( $nbiter -1))
```

This first part of the code extract the number of line in the given file. Because the Linux command `head` and `tail` are not optimal when the file has more than 495 lines it is necessary to divide the original file in subfiles whose number of lines does not exceed that value.

```
#condition the file for the next command
```

```
gawk −F"␣" '{print $1}' data/uY.dat > data/tempo
sed '494d' data/tempo > data/temp
rm data/tempo
mv data/temp data/tempo


#split the file to be efficient with the command head
csplit −f data/temp_ −sk −n 1 data/tempo 494 {$nbiter2}
```

Once the file are divided in temporary files `temp_` , the time lines are extracted from each of these files and stacked up in the file `time` .

```
#take the data at one line
for  ((j=1;j<=493;j=j+2))
do
head −$j data/temp_0 | tail −1 >> data/time
done


#for the rest
for  ((k=1;k<=$nbiter2;k=k+1))
do
for  ((j=1;j<=494;j=j+2))
do
head −$j data/temp_$k | tail −1 >> data/time
done
done
```

After computation the `temp_` files are deleted.

```
#delete temporary files
rm data/temp*
```

76

This script works fast even on huge files. For instance a 1GB file is treated in less than 1 minute with Intel Xeon processor. One may remark that the CA code should write the time separately for the rest of the data. However this would not change the problem because the file needs separators to isolate computation at each step. Moreover it is more robust to have the data and the displacement together for any verification. Finally it is better to have a file with more data than necessary and change a the script than changing the CA code and compile it which time consuming.

REFERENCES

[1] ACHENBACH, J. D., *Structural Health Monitoring with piezoelectric wafer active sensors*. Academic Press, 2008.

[2] ALLEYNE and CAWLEY, "A two-dimensional fourier transform method for the measurement of propagating multimode signals," *Journal of the Acoustical Society of America*, vol. 93, pp. 1159–1168, March 1991.

[3] ASME 2008 International Design Engineering Technical Conference & Computers and Information in Enginerering Conference, *A cellular automata modelimg approach for continuum elastodynamics*, (Brooklyn, New York, USA), August 2008.

[4] BLACKSHIRE, J. L., SATHISH, S., NA, J., and FROUIN, J., "Nonlinear laser ultrasonic measurements of localized fatigue damage," *Review of Quantitative Nondestructive Evaluation*, vol. 22, pp. 1479–1487, 2003.

[5] BRAUN, M. R., "Characterization of nonlinearity parameters in an elastic material with quadratic nonlinearity with a complex wave field," Master's thesis, School of Civil and Environmental Engineering, Georgia Institute of Technology, December 2008.

[6] DE LIMA, W. J. and HAMILTON, M. F., "Finite amplitude waves in isotropic elastic waveguite with arbitrary constant cross-sectional area," *Wave Motion 41*, 2005.

[7] GIURGIUTIU, V., *Wave propagation in elastic solids*. North Holland Elsevier, 1975.

[8] GRAFF, K. F., *Wave motion in elastic solids*. Dover, 1975.

[9] HAMILTON, M. F. and BLACKSTOCK, D. T., *Nonlinear Acoustics: Theory and Applications*. Academic Press, 1998.

[10] KIM, J.-Y., JACOBS, L. J., QU, J., and LITTLES, J. W., "Experimental characterization of fatigue damage in a nickel-base superalloy using nonlinear ultrasonic waves," *Journal of Acoustical Society of America*, vol. 3, pp. 1266–1273, September 2006.

[11] LANDAU, L. and LIFSCHITZ, E., *Théorie de l'élasticité*. Editions MIR, 1967.

[12] LEAMY, M. J., "Application of cellular automata modeling to seismic elastodynamics," *International Journal of Solids and Structures*, vol. 45, pp. 4835–4849, September 2008.

[13] LEMAITRE, J. and CHABOCHE, J.-L., *Mécanique des matériaux solides*. Dunod, 2nd ed., 2004.

[14] MCCALL, K. R., "Theoretical study of nonlinear elastic wave propagation," *Journal of Geophysical Research*, vol. 99, pp. 2591–2600, 1994.

[15] MORVAN, B., WILKIE-CHANCELLIER, N., DUFLO, H., TINEL, A., and DUCLOS, J., "Lamb wave reflection at the free edge of a plate," *Journal of the Acoustical Society of America*, vol. 113, pp. 1417–1425, March 2003.

[16] POLYAKOVA, A. L., *Non-linear effects in a solid*. Soviet Physics - Solid State, 1964.

[17] SHAPIRO, N. M., CAMPILLO, M., MARGERIN, L., SINGH, S., KOSTOGLODOV, V., and PACHECO, J., "The energy partitioning and the diffusive character of the seismic coda," *Bulletin of the Seismological Society of America*, vol. 90, pp. 655–665, June 2000.

[18] TANNEHILL, J. C., ANDERSON, D. A., and PLETCHER, R. H., *Computational Fluid Mechanics and Heat Transfer*. Taylor & Francis, second ed., 1997.

[19] VIKTOROV, I. A., *Rayleigh and Lamb Waves, Physical Theory and Applications*. Plenum Press, 1967.

[20] WEAVER, R. L., "Diffuse waves in finite plates," *Journal of Sound and Vibration*, vol. 94, no. 3, pp. 319–335, 1984.

INDEX